LNGS-LOI 20/99
CERN/SPSC 99-24
SPSC/M636
August 26, 1999

Progress Report

towards an Experiment to Study

Atmospheric Neutrino Oscillations

with a

Massive Magnetized Iron Detector

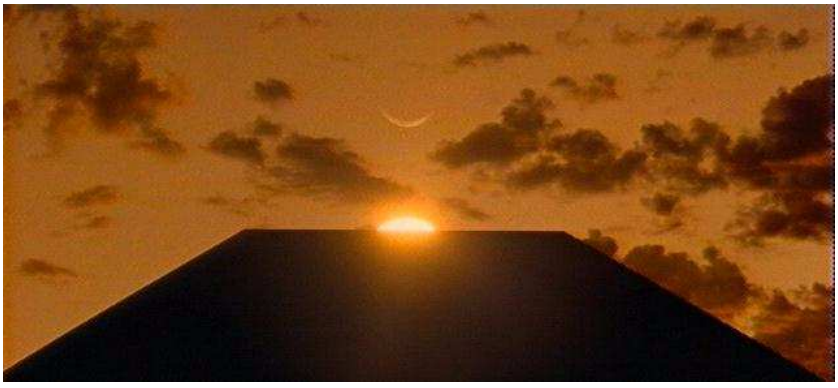

The MONOLITH Project

Massive **O**bservatory for **N**eutrino **O**scillations or **LI**mits on **TH**eir existence

M. Ambrosio[1] M. Amelchakov[2] P. Antonioli[3] E. Aprile[4] C. Aramo[1]
V. Aynutdinov[2] G. Bari[3] R. Benaceur[5] G. Bencivenni[6] G. Bologna[6,7]
M. Bonesini[8] G. Bruni[3] N. Bruski[9] F.W. Büsser[10] J.E. Campagne[11]
D. Chernov[2] M. Chemarin[12] A. Curioni[4] L. Chaussard[12] Y. Déclais[12]
D. Duchesneau[13] A. Ezubchenko[2] J. Favier[13] D. Frekers[9] P. Galeotti[7,14]
A. Garfagnini[10] A. Geiser[10] F. Gharbi[5] P. Giusti[3] D. Golubkov[2]
N. Goloubev[15] S. Gninenko[15] C. Gustavino[16] G. Heinzelmann[10]
R. Hermel[13] K. Hoepfner[10] P. Jonsson[12] S. Katsanevas[12] V. Kindin[2]
M. Kirsanov[15] R. Klanner[10] B. Koppitz[10] R. Kokoulin[2] K. Kompaniets[2]
A. Konovalov[2] A. Kovzelev[15] I. Laktineh[12] G. Mannocchi[6,14] J. Marteau[12]
B. Merkel[11] P. Monacelli[17,16] G. Moret[12] F. Murtas[6] G.P. Murtas[6]
R. Nania[3] B. Naroska[10] P. Negri[8] A. Ordine[1] M. Paganoni[8] A. Pesci[3]
H. Pessard[13] L. Periale[14] A. Petrukhin[2] P. Picchi[6,14,7] A. Pullia[8]
S. Ragazzi*,[8] N. Redaelli[8] J.P. Repellin[11] D. Rondeshagen[9] F. Ronga[6]
G. Sartorelli[3] L. Satta[6,18] W. Schmidt-Parzefall[10] M. Spinetti[6] C. Souga[5]
T. Tabarelli de Fatis[8] F. Terranova[8] A. Trabelsi[5] G. Trinchero[14]
R. van Staa[10] J.J. Veillet[11] B. Villone[14] L. Votano[6] K. Winter[19]
H.J. Wörtche[9] T. Wolff[9] E. Yanson[2] I. Yashin[2]

* contact person

[1]INFN, Sezione di Napoli, Napoli, Italy
[2]Moscow Engineering Physics Insitute, Moscow, Russia
[3]Bologna University and INFN, Bologna, Italy
[4]Physics Department and Columbia Astrophysics Laboratory, Columbia University, New York, NY 10027, USA
[5]Laboratoire de Physique Nucléaire et de Physique des Particules, Faculté des Sciences de Tunis, Tunis, Tunisia
[6]Laboratori Nazionali di Frascati, INFN, Frascati, Italy
[7]University of Torino, Torino, Italy
[8]Dipartimento di Fisica, Università di Milano Bicocca and INFN Sezione di Milano, Italy
[9]Münster University, Münster, Germany
[10]Hamburg University, Hamburg, Germany
[11]Laboratoire de l'Accélérateur Linéaire (LAL), IN2P3-CNRS and Université Paris-Sud, Orsay, France
[12]Institut de Physique Nucléaire de Lyon (IPNL), IN2P3-CNRS and Université Claude Bernard, Villeurbanne, France
[13]Laboratoire d'Annecy-le-Vieux de Physique des Particules (LAPP), IN2P3-CNRS and Université de Savoie, Annecy, France
[14]Istituto di Cosmogeofisica, CNR, Torino, Italy
[15]Institute for Nuclear Research (INR), Moscow, Russia
[16]Laboratori Nazionali di Gran Sasso, INFN, Assergi, Italy
[17]Physics Depart. University of L'Aquila and INFN, L'Aquila, Italy
[18]Rome University, Rome, Italy
[19]Humboldt University Berlin, Berlin, Germany

Contents

Chapter 1

Introduction

The question whether neutrinos are massive, and hence the question of the existence of neutrino oscillations, is currently one of the main unsettled challenges in physics. All experiments measuring the flux of solar neutrinos observe a deficit compared to the prediction of solar models [1]. The ratio of muon to electron events observed in atmospheric neutrino interactions is measured by most experiments to be less than expected from models of cosmic ray interactions in the atmosphere [2]. The measurement of the up/down asymmetry of this ratio by the Super-Kamiokande collaboration [3] is generally considered to be the strongest evidence for neutrino oscillations so far. Furthermore, the LSND experiment has observed possible oscillation signals in the $\bar{\nu}_\mu - \bar{\nu}_e$ and $\nu_\mu - \nu_e$ channels [4]. Finally, neutrinos are a candidate for a partial solution to the missing dark matter problem [5] if at least one mass eigenstate lies in the eV range. These observations make the study of neutrino oscillations a very worthwhile endeavour.

While the cumulative evidence for neutrino oscillations is very striking, the final proof that the observed anomalies are actually due to neutrino oscillations is still outstanding. In particular, the current observations of atmospheric neutrinos are all consistent with the hypothesis of maximal ν_μ oscillations, but do not yet fully exclude alternative non-Standard Model explanations [6][7].

The main physics goal of the MONOLITH experiment is to establish the occurrence of neutrino oscillations in atmospheric neutrinos through the explicit observation of the first oscillation minimum in ν_μ disappearance [8], to investigate and presumably exclude alternative explanations, and to significantly improve the measurement of the oscillation parameters with respect to previous measurements. The experimental design, a massive iron calorimeter, has been inspired by earlier detector studies [9][10]. In particular, the detector concept of ref. [9] has been extended to be sensitive to the full parameter range allowed by current experiments. This is achieved mainly through the addition of a strong magnetic field, which is a novel feature among atmospheric neutrino detectors. The additional charge and momentum measurement of muons from charged current (CC) events also allows unique systematic studies of the atmospheric neutrino flux, and the search for potential matter effects in neutrino oscillations.

Provided that the neutrino oscillation hypothesis is confirmed, the second goal of the experiment is to further investigate the nature of these oscillations. Depending on the oscillation parameters, oscillations into active (ν_τ) or sterile (ν_s) neutrinos can be distinguished through their different effects on the up/down ratio of neutral current (NC)-like events, and/or through the presence or absence of matter effects yielding a distortion

of the observed oscillation pattern as a function of energy or muon charge.

For this experiment we have designed a baseline option which has been optimized for the detection of atmospheric neutrinos and can achieve these physics goals. This baseline design would have limited sensitivity to the neutrino beam from CERN. Detector options which would improve this sensitivity without compromising the atmospheric neutrino performance are being investigated.

In its baseline version, a first part of the detector could be operational in 2002/2003. The physics results described in the following chapters correspond to an exposure of 4 years with the full detector.

This document is organized as follows:

Chapter 2 treats in more detail the physics motivation outlined above. The detection principle of the proposed measurements is discussed in chapter 3, therefore defining the detector requirements. The implementation of the baseline detector option satisfying these requirements is presented in chapter 4, and chapter 5 describes the corresponding expected analysis results. Physics issues related to long baseline neutrino beams are briefly outlined in chapter 6. Finally, cost estimates and time scales are reviewed in chapter 7, and chapter 8 summarizes the general conclusions.

Chapter 2

Physics Motivation

2.1 Physics context

The main motivation for the design of this experiment is to clarify some of the questions left open by the current and planned atmospheric and long baseline neutrino experiments. The current measurement of the atmospheric neutrino anomaly by Super-Kamiokande [3], supported by other atmospheric neutrino measurements, yields *"evidence for oscillation of atmospheric neutrinos"* [3]. However, the experimental resolution is too poor to clearly resolve the oscillation pattern, such that alternative explanations like neutrino decay can not be excluded [7]. Furthermore, while the pure $\nu_\mu \to \nu_e$ oscillation hypothesis is disfavoured both by the atmospheric neutrino data [3] and by the results of the CHOOZ reactor experiment [11], the question whether the main effect is due to $\nu_\mu \to \nu_\tau$ or $\nu_\mu \to \nu_s$ oscillations is essentially unsettled. Here, ν_s is a hypothetical "sterile" neutrino, which is relevant for atmospheric neutrinos in many oscillation models [12] and might be needed to simultaneously explain all known neutrino anomalies. This point will be developed further in section 2.3.

Promising new insights are expected from new long baseline neutrino beam programs. K2K [13], the first long baseline accelerator neutrino experiment, started this year in Japan. The sensitivity for ν_μ disappearance expected after 3 years at nominal intensity extends down to between 2 and 3×10^{-3} eV^2 (figure 2.1). It does not quite cover the Δm^2 range indicated by the present atmospheric neutrino results. Pure $\nu_\mu \to \nu_e$ oscillations are already strongly disfavoured by Super-Kamiokande atmospheric neutrino data.

If K2K observes a ν_μ disappearance signal, the type of oscillation, ν_τ or ν_s, will not be determined, and the oscillation pattern will again not be fully resolved. However, such a disappearance signal would strengthen the neutrino oscillation hypothesis, and indicate oscillation parameters in the upper half of the Δm^2 range allowed by Super-Kamiokande. Conversely, the absence of a clear signal would favour the lower half of this range. A firm result on this issue can be expected by the end of 2001.

The construction of the American long baseline programme NUMI [14] started this year. MINOS is a 5.4 kton (3.3 kton fiducial mass) detector dedicated to ν_μ disappearance. The beam is scheduled to be commissioned in the last quarter of 2002, and the detector is planned to be partially operational in 2002, and fully completed in the first quarter of 2003. The Soudan-2 detector [15] will also be running in the NUMI beam, with a mass of less than a kiloton but a very fine granularity.

The expected performance of MINOS for 10 kty is outlined in figure 2.1. The exper-

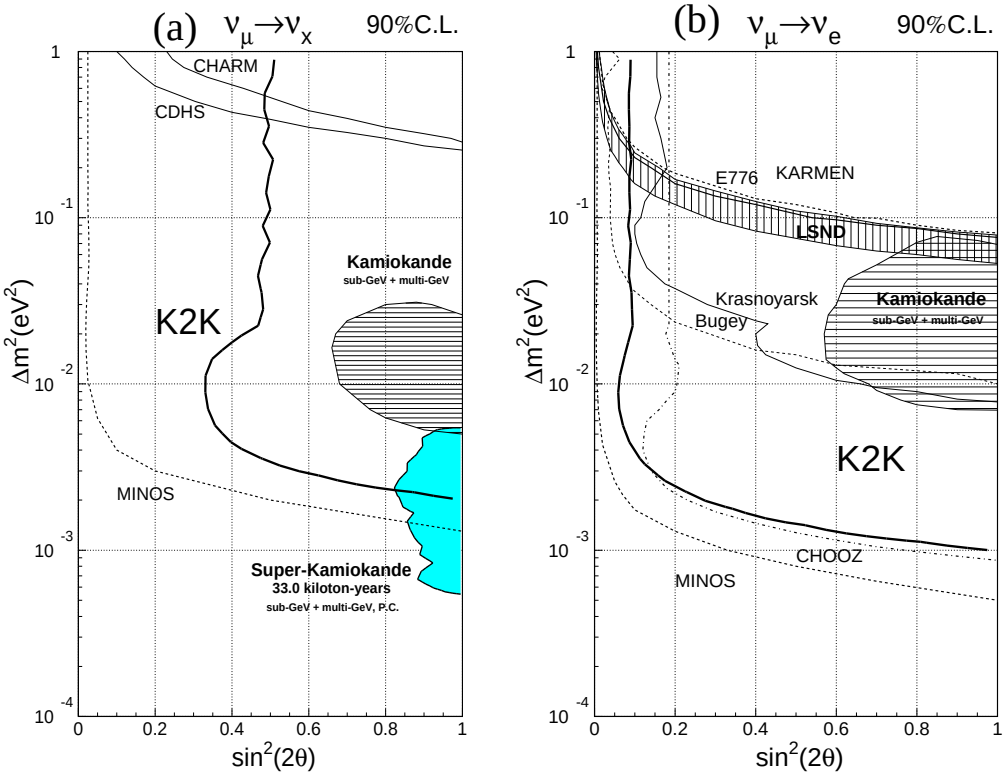

Figure 2.1: Expected sensitivity for K2K [13] and MINOS [14] (reference beam, for low energy beam see text) for ν_μ disappearance (a) and for $\nu_\mu \to \nu_e$ (b) after 3 years of data taking. Published results from Super-Kamiokande [3], Kamiokande [16] and other experiments [11, 4, 17] are also shown.

imental sensitivity reaches 2×10^{-3} eV^2 in Δm^2 with the reference beam ($< E_\nu > \sim 17$ GeV), and 6×10^{-4} eV^2 with a low energy version of the beam called PH2(low) ($< E_\nu > \sim 5$ GeV); the corresponding discovery contour ($4\ \sigma$) goes down to 1×10^{-3} eV^2.

Finally, the CERN neutrino beam to Gran Sasso (CNGS) [18] is scheduled for potential approval by the end of this year, to become operational in 2005, i.e. after the startup of the proposed atmospheric neutrino experiment. A brief discussion of issues related to this beam can be found in chapter 6. The prospects for beams from muon storage rings are also discussed in this chapter.

2.2 Observation of neutrino oscillation pattern

In the two flavour approximation, the survival probability for neutrino oscillations in vacuum can be expressed by the well known formula

$$P(L/E) = 1 - \sin^2(2\Theta)\ \sin^2(1.27\ \Delta m^2\ L/E) \tag{2.1}$$

where L is the distance travelled in km, E is the neutrino energy in GeV, Θ is the neutrino mixing angle, and Δm^2 is the difference of the mass square eigenvalues expressed in eV^2.

However, none of the experiments which have yielded indications for neutrino oscillations have so far succeeded to measure an actual sinusoidal oscillation pattern. Figure 2.2 shows the L/E distribution published by Super-Kamiokande [3] compared to the expectation for neutrino oscillations and to a functional form suggested by a recent neutrino decay model [7]. Once the detector resolution is taken into account, the two hypotheses are essentially indistinguishable [7]. Even if one accepts the existence of neutrino oscillations based on the current evidence, a more precise measurement of the oscillation pattern is necessary to actually prove the oscillation hypothesis for atmospheric neutrinos.

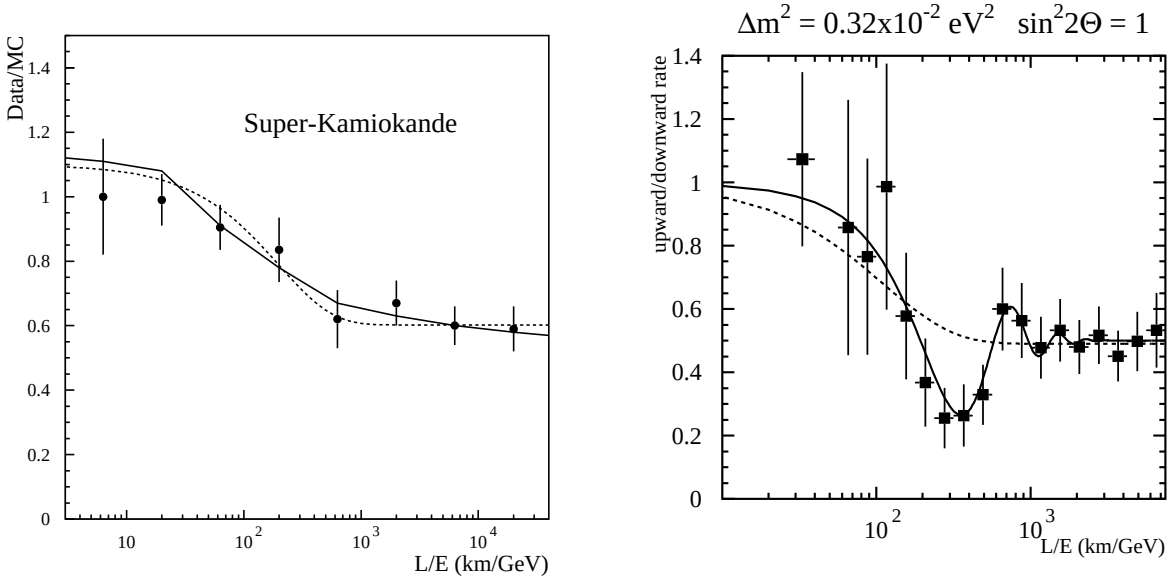

Figure 2.2: *Left*: L/E distribution from Super-Kamiokande [3] compared to the best fit oscillation hypothesis (including detector resolution, continous line), and to a parametrization corresponding to the neutrino decay model of ref. [7] (without detector resolution, dashed line). *Right*: L/E distribution to be expected from MONOLITH (see Chapter 5) for $\Delta m^2 = 3.2 \times 10^{-3}$ eV^2 compared to the best fit oscillation hypothesis (including detector resolution, continous line), and to a parametrization corresponding to the neutrino decay model of ref. [7] (without detector resolution, dashed line).

The proposed MONOLITH experiment is explicitly designed to fill this gap. Having a similar mass as Super-Kamiokande, significantly larger acceptance at high neutrino energies and better L/E resolution, the experiment is optimized to observe the full first oscillation minimum, i.e. half an oscillation period, in ν_μ disappearance (chapter 3). Therefore, the oscillation hypothesis can be clearly distinguished from other hypothesis which yield a pure threshold behaviour (figure 2.2).

Furthermore, the sensitivity is almost independent of the oscillation parameters (chapter 5). This is in contrast to MINOS, which can do a similar measurement at the highest allowed Δm^2 if the low energy beam is used [19], but can observe only a quarter oscillation period or less in the lower Δm^2 range.

Finally, the better L/E resolution can be used to improve the measurement of the oscillation parameters by almost an order of magnitude with respect to the present precision

over the full allowed range (see fig. 5.6 in chapter 5).

2.3 Distinction of $\nu_\mu \rightarrow \nu_\tau$ vs. $\nu_\mu \rightarrow \nu_s$

If the current indications for three independent Δm^2 are confirmed, the only way out is the introduction of at least a fourth neutrino. Taking into account the LEP results [20] on the number of neutrinos, any extra neutrinos must be either very massive ($m_\nu > M_Z/2$) or sterile with respect to weak interactions (e.g. a right-handed neutrino or left-handed antineutrino). Present experiments can not clearly distinguish oscillations with sterile neutrinos from standard flavour oscillations for either atmospheric [21] or solar [1] neutrinos. $\nu - \nu_s$ oscillations are therefore allowed in both cases.

Since the existence of one or more light sterile neutrinos would be evidence for new physics, proving or disproving the $\nu_\mu - \nu_\tau$ oscillation hypothesis for atmospheric neutrinos is a crucial issue. Furthermore, it would exclude or confirm a large class of neutrino oscillation models (see e.g. [22] and references therein). The observation of τ appearance in long baseline beams would be the most direct evidence for $\nu_\mu - \nu_\tau$ oscillations, but potentially leaves some loopholes for the interpretation of the atmospheric neutrino results [23]. These loopholes could be closed through a direct $\nu_\mu \rightarrow \nu_\tau$ vs. $\nu_\mu \rightarrow \nu_s$ distinction in atmospheric neutrino experiments.

The Super-Kamiokande experiment is trying to disentangle between the ν_s and ν_τ oscillation hypotheses using several approaches. The current measurement [24] of the double ratio of "π^o" events [25]

$$\frac{(\pi^0/e)_{data}}{(\pi^0/e)_{MC}} = 1.00 \pm 0.06(stat) \pm 0.23(syst) \tag{2.2}$$

is compatible with both solutions (the expected ratio is 1 for ν_τ and ≈ 0.76 for ν_s). This measurement is mainly limited by systematic uncertainties on the cross section (currently 20%). The K2K experiment, with the near detector, will allow to reduce this systematic error, but even reducing the total uncertainty to 10% is unlikely to yield a 3σ evidence [23]. Also the study of the π^o up/down asymmetry [26] is unlikely to reach a 3σ significance in the discrimination between the two hypotheses.

The second approach is based on potential matter effects affecting $\nu_\mu \rightarrow \nu_s$ oscillation inside the Earth. Matter effects can radically modify the neutrino oscillation pattern with respect to oscillations in vacuum [27]. These effects occur for oscillations involving neutrinos having different interactions with matter. So matter effects are absent for $\nu_\mu \rightarrow \nu_\tau$ oscillations and present for $\nu_\mu \rightarrow \nu_e$ and $\nu_\mu \rightarrow \nu_s$ oscillations. Due to these effects, the expected shape of the zenith distribution of up-going muons is different for $\cos(\theta) \leq$ -0.4, as pointed out in [28].

The Super-Kamiokande collaboration [24] presented a very preliminary analysis disfavoring the $\nu_\mu \rightarrow \nu_s$ hypothesis at the 2σ level using this approach, and dividing the angular distribution for upward going muons into two bins. Using the complete angular distribution MACRO has found a similar indication [29]. More complicated scenarios with 3 flavour oscillations can not be excluded with the existing data.

The MONOLITH experiment can exploit the spirit of both approaches to improve on these measurements. The first technique, based on the up/down ratio of high energy "NC-like" events (including τ appearance), is explained in chapters 3 and 5. This up/down

study will be much less affected by systematic uncertainties on cross sections and/or detector acceptance than NC/CC studies. Depending on Δm^2, a separation of the ν_τ and ν_s hypotheses of up to 3 σ is within the reach of the experiment.

The second technique, based on potential matter effects, is only briefly discussed below, since detailed simulation results are not yet available. An analysis similar to the one recently performed by Super-Kamiokande [24] can be carried out on the sum of the neutrino and antineutrino components of the atmospheric neutrinos, using the fact that $\nu_\mu - \nu_s$ oscillations get suppressed at high energies. In MONOLITH, the significance of the result should be improved by the higher acceptance for high energy contained and semi-contained events, and its capability to measure the momenta of upward through-going muons. Furthermore, the predicted shape and position of the first oscillation minimum (section 2.2) becomes energy and angle-dependent, yielding an additional handle for the $\nu_\tau - \nu_s$ discrimination.

Moreover, with the exception of the special case of maximal mixing ($\sin^2(2\Theta) = 1$), neutrinos and antineutrinos have different oscillation parameters in matter. The effective mixing in matter becomes maximal when the resonance condition [30] is satisfied. This is possible for antineutrinos (neutrinos) when Δm^2 is positive (negative). Additional resonance effects are possible if the matter density varies along the neutrino path [31]. So in the case of non-maximal oscillations with matter effects we expect a change in the observed $\nu_\mu/\bar{\nu}_\mu$ ratio (fig. 2.3). This phenomenon could be used to measure the sign of Δm^2. In this context we can use the MONOLITH capability to separate the ν and $\bar{\nu}$ component and to measure muon momenta up to several hundred GeV.

As a first outlook into this kind of analysis, we show results of computations for up-going muons. We expect about 250 events per year with a muon threshold larger than 1 GeV (in the absence of oscillations) produced by neutrino interactions external to the detector and coming from below.

Figure 2.3 shows the ratio:

$$R = \frac{N_{\mu NoOscillation}}{N_\mu} \tag{2.3}$$

for μ^- (neutrinos) and μ^+ (anti-neutrinos) as a function of angle and energy for Δm^2=0.005 eV^2 and $\sin^2(2\Theta) = 0.8$. There is a clear difference between neutrinos and antineutrinos. The size and sign of this difference depends on the sign of Δm^2. Of course the difference is zero for maximal mixing. However we have verified that even at a value of $\sin^2(2\Theta) = 0.95$ there is a measurable difference between μ^- and μ^+.

Finally, matter effects are also present in the case of a significant contribution from $\nu_\mu - \nu_e$ oscillations. Taking into account the CHOOZ limit [11], the expected effects are generally small. A possible exception could be the observation of a neutrino/antineutrino asymmetry predicted by tri-maximal mixing models [32], which are currently not yet completely excluded.

The full statistical analysis of the implication of the matter effects with charge recognition is in progress both for external and internal events.

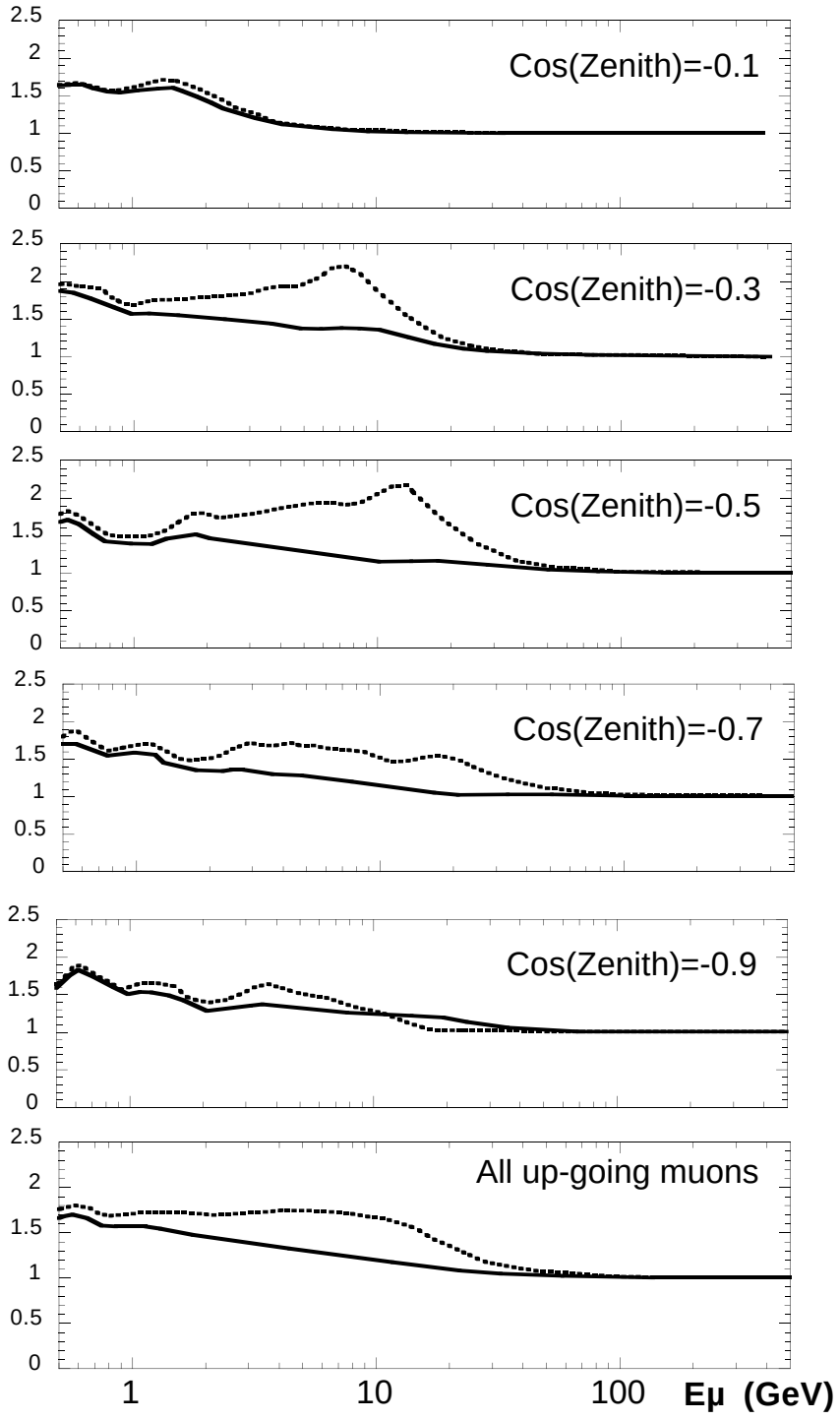

Figure 2.3: Ratio $R = \frac{N_{\mu NoOscillation}}{N_{\mu}}$ for upward going muons in 5 angular bins as function of the energy for $\nu_\mu - \nu_s$ oscillations with Δm^2=0.005 eV^2 and $\sin^2(2\Theta) = 0.8$. Matter effects are included. The ratio is shown separately for μ^- (continous line) and μ^+ (dashed line).

2.4 Cosmic ray muon studies

MONOLITH is also well suited for the study of muons from cosmic rays. Detailed simulation studies are not yet available, but some important aspects are outlined below.

The spectrum of primary cosmic ray particles observed in extensive air shower (EAS) investigations is well described by a power law over many orders of magnitude in energy. However, it exhibits a well known change in slope (the so called "knee") around $10^{15} - 10^{16}$ eV (1-10 PeV). In nucleon-nucleon collisions, PeV energies in the laboratory system correspond to center of mass energies in the TeV region, where new physics and new (heavy) particles are predicted by various theoretical models. Above 2 TeV these energies are out of the reach of current accelerators.

There are two main possibilities for the explanation of the knee: a change of the primary spectrum (and/or composition), or the appearance of new processes in very high energy interactions. Today most investigators support the first point of view. However, the second option remains possible (see for example [34]). In this case, the knee would be explained by missing energy carried away by leptons which are not or incompletely detected by EAS arrays: neutrinos and very high energy muons. These could originate from the decay of any new particles in the TeV mass region (Supersymmetry, Compositeness, heavy Higgs, ...) produced with a large cross section of order tens of mb. It was pointed out recently [33] that a good possibility to find such new particles in cosmic rays is to perform a measurement of the muon energy spectrum. Therefore the direct measurement of this spectrum in the multi-TeV region (fig. 2.4) can yield very important information about the nature of the knee.

From the point of view of cosmic ray muon investigations MONOLITH will be the first spectrometer in the world for the measurements of muon energies in the interval of hundreds of TeV that uses a pair meter technique [35]. This technique is based on the multiple production of secondary cascade showers (mostly from e^+e^- pair production) along the muon trajectory over a very large number of radiation lengths (more than 500 X_0 for MONOLITH, which is needed to reach an energy resolution of about 50%). The important feature of the technique is the absence of an upper limit on the measurable muon energy. The detector will have an effective acceptance several orders of magnitude larger than the biggest previous magnetic spectrometers [36]. The expected integral rate of standard cosmic ray muons in MONOLITH is shown in fig. 2.4. It was obtained from the surface muon energy spectrum, taking into account that muons reaching the Gran Sasso laboratory lose on average 2/3 of their energy. The expected additional contribution from heavy particle decays needed to explain the knee is also shown. The drastic change of the muon energy spectrum around 100 TeV would be an excellent signature of new processes.

Even in the absence of such a contribution, simultaneous measurements of the energy and zenith angle of individual muons open new ways of investigating primary cosmic ray interactions as well as their particle spectrum and composition. Inelastic scattering processes of high energy muons can also be studied.

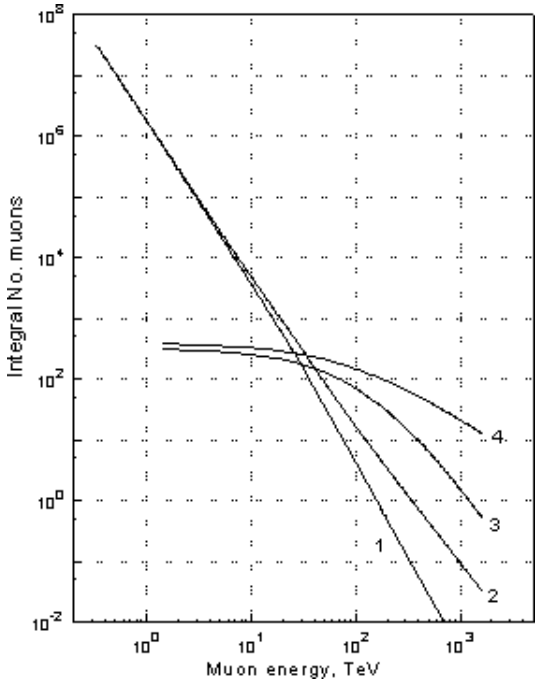

Figure 2.4: Integral number of cosmic ray muons from various processes, which will be detected by MONOLITH in 3 years: 1 - π, K decays only; 2 - π, K decays and "prompt" muons for a ratio $R_{\mu/\pi} \sim 10^{-3}$; 3 and 4 - lower and upper limits for muons from heavy particle decays to explain the "knee" [33] (see text).

Chapter 3

Detection principle

3.1 Introduction

The physics goals of the experiment are to firmly establish/disprove the evidence of neutrino oscillations reported by the Super-Kamiokande collaboration [3], measure the oscillation parameters and clarify the nature of the oscillation mechanism. This programme can be accomplished in an experiment on atmospheric neutrinos, exploiting the high energy component of the atmospheric neutrino fluxes. In this context, the following techniques have been mainly considered:

- detection of an oscillation pattern in the L/E spectrum from the comparison of upward and downward rates of charged current interactions of high energy muon neutrinos;
- comparison of upward and downward rates of muon-less events of high energy;
- study of matter effects on high energy up-going neutrinos.

The first technique ("ν_μ disappearance"), already investigated in [8, 9], where a high density and large mass tracking calorimeter was proposed, requires the capability to reconstruct in each event the L/E ratio of the neutrino path-length to its energy. Oscillations of muon neutrinos would manifest themselves in a modulation of the L/E spectrum, from which the oscillation parameters can be measured. This technique, formerly suggested in [37], has sensitivity to ν_μ oscillations with $\Delta m^2 > 6 \times 10^{-5}$ eV^2 and mixing near to maximal and fully covers the region of oscillation parameters suggested by Super-Kamiokande results [9]. In the present proposal, an increased sensitivity in the region of $\Delta m^2 \geq 3 \times 10^{-3}$ eV^2 with respect to past studies is achieved by means of a magnetised calorimeter.

The second ("ν_τ appearance") technique can shed light on the nature of the oscillation mechanism, by discriminating between the hypothesis of oscillations into a sterile or a tau neutrino. The ν_τ appearance method can also be exploited in a large mass calorimeter [9], where the appearance of ν_τ interactions contributing to muon-less events of high energy can be searched for. This method is effective for $\Delta m^2 > 3 \times 10^{-3}$ eV^2.

Both the ν_μ disappearance and the ν_τ appearance methods are to a large extent independent of predictions of neutrino event rates, since they rely on the comparison of rates induced by a near (downward going) and a far (upward going) neutrino sources.

Besides these "model independent" methods, additional information on the oscillation mechanism can be obtained from the study of potential matter effects related to the propagation of upgoing neutrinos through the Earth. In particular, as discussed in Chapter 2, evidence of matter effects could be detected from the separate measurement of μ^+ and μ^- rates induced by high energy upgoing muon neutrinos and anti-neutrinos. To accomplish this, the unique feature of the magnetised detector proposed here of measuring the muon charge and hence flag the leptonic charge of the muon neutrino can be exploited. The potential of this latter method to clarify the oscillation mechanism will not be further addressed in this report, since a complete study of all the experimental aspects involved in this measurement has not been performed yet.

In the following a detailed description of the ν_μ disappearance and of the ν_τ appearance methods, of the requirements on the detector performance and of the implications for the detector design is presented.

3.2 Disappearance of muon neutrinos

Atmospheric neutrino fluxes are not in general up/down symmetric. However, the up/down asymmetry, which is mainly due to geomagnetic effects, is reduced to the percent level for neutrino energies above 1.5 GeV [38, 39]. At these energies, for $\Delta m^2 < 10^{-2}$ eV^2, as indicated by Super-Kamiokande results, downward muon neutrinos are almost unaffected by oscillations. Thus, they may constitute a *near* reference source. Upward neutrinos are instead affected by oscillations, since the L/E ratio of their path length over the energy ranges up to 10^4 km/GeV. Atmospheric neutrinos therefore represent an ideal case for a disappearance experiment, since one may study oscillations with a single detector and two sources: a *near* and a *far* one. The effects of oscillations are then searched comparing the L/E distribution for the upward neutrinos, which should be modulated by oscillations, with a reference distribution obtained from the downward neutrinos. For upward neutrinos the path length L is determined by their zenith angle as $L(\theta)$, while the reference distribution is obtained replacing the actual path length of downward neutrinos with the mirror-distance $L'(\theta) = L(\pi - \theta)$ (see Fig. 3.2).

According to the figure and given symmetry properties of the cosine, the neutrino path-length can therefore be estimated as $L(\theta) = R_{Earth}(\sqrt{1 - k^2 \sin^2\theta} - k|\cos\theta|)$, where $k = R_{Earth}/(R_{Earth} + \Delta R) \simeq 0.995$ and ΔR represents an average neutrino production height in the atmosphere. The ratio $N_{up}(L/E)/N_{down}(L'/E)$ will then correspond to the survival probability given, in case of oscillations, by eq. (2.1) (section 2.2). A smearing of the modulation is introduced by the finite L/E resolution of the detection method as discussed in the following and in chapter 5, where the analysis of simulated data is presented.

Some remarks are in order:

i) results obtained by this method (known as Picchi & Pietropaolo's [37]) are to a large extent insensitive to systematic effects arising from uncertainties in the knowledge of atmospheric fluxes, neutrino cross sections and detector inefficiencies.

ii) this method does not work with neutrinos at angles near to the horizontal ($|\cos\theta| < 0.07$), since the path lengths corresponding to a direction and its mirror-direction are of the same order.

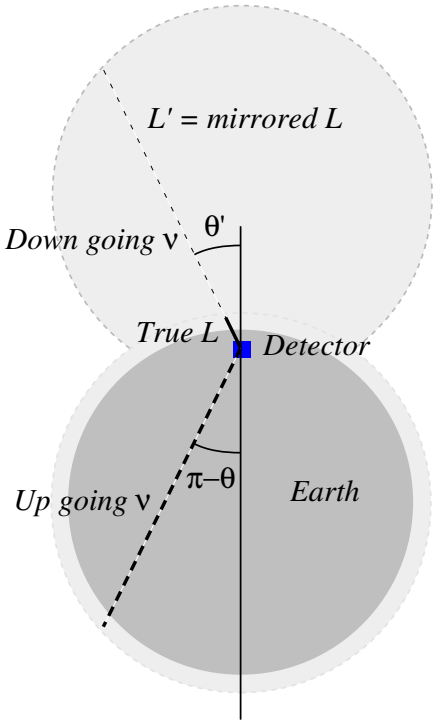

Figure 3.1: Artist's view of the mirror neutrino path length: downward going neutrinos (zenith angle $\theta < \pi/2$) are assigned the distance they would have travelled if $\theta = \pi - \theta$.

We also notice that if Δm^2 were larger than 10^{-2} eV^2 (Kamiokande region), upward neutrinos would be in almost complete oscillation, while the oscillation pattern would become detectable in the downward sample. In this limit, a mirror-distance $L'(\theta) = L(\pi - \theta)$ can be assigned to upward neutrinos, which can be used as a reference L/E distribution for downward neutrinos. In this case, due to the uncertain estimate of the neutrino path-length for downgoing neutrinos related to our ignorance of their production height in the atmosphere, there would be some model dependence in the determination of the oscillation parameters. Nonetheless, the observation of an oscillation pattern would still firmly test the oscillation hypothesis.

A more "standard" technique, based on the direct comparison of the measured rates of charged current ν_μ interactions to the predicted ones, could also be exploited over the full range of Δm^2 of interest. We however believe that the larger systematic uncertainties associated to this approach make it less attractive.

The outlined experimental method requires that the energy E and direction θ of the incoming neutrino be measured in each event. The latter, in the simplest experimental approach, can be estimated from the direction of the muon produced in the ν_μ charged-current interaction. The estimate of the neutrino energy E requires the measurement of the energy of the muon and of the hadrons produced in the interaction. In order to make the oscillation pattern detectable, the experimental requirement is that L/E be measured with a FWHM error smaller than half of the modulation period. This translates into

requirements on the energy and angular resolutions of the detector or, more generally, of the experimental approach. As a general feature the resolution on L/E improves at high energies, mostly because the muon direction gives an improved estimate of the neutrino direction. Thus the ability to measure high momentum muons (in the multi-GeV range), which is rather limited in the on-going atmospheric neutrino experiments, would be particularly rewarding.

These arguments led to consider in previous papers [9] a large mass and high-density tracking calorimeter as a suitable detector. A large mass is necessary to provide enough neutrino interaction rate at high energy, while the high-density provided muon energy measurement by range. A sizeable increase in sensitivity for Δm^2 larger than 3×10^{-3} eV^2, can be achieved with a detector of the same structure as in [9], with the addition of a magnetic field. At reasonable costs, this improves muon acceptance at high momenta, and correspondingly efficiency at small L/E.

This choice puts emphasis on the muon reconstruction. The high-density provides good π/μ separation, hence capability to select a pure ν_μ-CC sample, while the measurement of the muon energy and direction can be obtained with good precision. On the other hand, even with a coarse resolution to hadrons, the overall L/E resolution can be controlled by selection of neutrino interactions of limited inelasticity for small neutrino energies. This is best seen from the expression of the relative L/E resolution:

$$\frac{\sigma^2_{L/E}}{(L/E)^2} = \frac{\sigma^2_E}{E^2} + \frac{\sigma^2_L}{L^2} \tag{3.1}$$

$$\simeq \frac{\sigma^2_{E_\mu}}{E^2_\mu}(1-y)^2 + \frac{\sigma^2_{E_h}}{E^2_h}y^2 + \tan^2\theta\sigma^2_\theta; \tag{3.2}$$

where E, E_μ and E_h are the neutrino, muon and hadronic energies, $y = E_h/E$ is the inelasticity of the interaction and θ is the zenith angle of the incoming neutrino. Events of limited inelasticity have both a good resolution on the neutrino energy, dominated by the resolution on the muon energy, and on the neutrino direction estimate from the muon direction. Equation (3.2) implies that acceptance at small L/E can only be achieved by recovering events of high energy, since near the horizontal (at small L) the L/E resolution is intrinsically limited by the knowledge of the neutrino direction. The detector does therefore not need to be fully isotropic. Improvement of the L/E resolution through better hadron reconstruction would only be possible with a calorimeter of much higher granularity, which would increase costs, reduce muon containment and conflict with the requirement of a large mass.

In addition to these requirements on the L/E resolution, the experimental apparatus should guarantee the identification of the neutrino flight direction. If the interaction vertex is not identified, this requirement is very stringent and translates into a requirement for the identification of the muon flight direction with high efficiency and purity. Different techniques can be envisaged, based on the increase of curvature along the track in the magnetic field, on multiple scattering along the track or on time-of-flight measurements. The latter technique is more effective and allows almost perfect up/down discrimination of the relevant ν_μ-CC events for timing resolution of order 1 ns. A precise time-of-flight along the muon track will also be of utmost importance in the rejection of the cosmic muon background in the sample of partially contained ν_μ-CC events.

3.3 Appearance of tau neutrinos

If evidence of neutrino oscillation from the study of ν_μ disappearance is obtained, a method based on τ appearance can be used to discriminate between oscillations $\nu_\mu \to \nu_\tau$ and $\nu_\mu \to \nu_s$. This method consists in measuring the upward/downward asymmetry of muon-less events as a function of the visible energy.

For $\Delta m^2 \leq 10^{-2}$ eV^2, oscillations of ν_μ into ν_τ would in fact result in an excess of muon-less events produced by upward neutrinos with respect to muon-less downward, since charged-current ν_τ interactions would contribute to the muon-less event sample, due to the large τ branching ratio into muon-less channels. Moreover, due to threshold effect on τ production, this excess would be important at high energy. Oscillations into a sterile neutrino would instead result in a depletion of upward muon-less events. Discrimination between $\nu_\mu \to \nu_\tau$ and $\nu_\mu \to \nu_s$ is thus obtained from a study of the asymmetry of upward to downward muon-less events. Because this method works with the high energy component of atmospheric neutrinos, it becomes effective for relatively large values of Δm^2 ($\geq 3 \times 10^{-3}$ eV^2).

Table 3.1 shows the integrated rates of neutrino CC interactions for $\cos\theta < 0$ (upward neutrinos) and for $\cos\theta < -0.5$. The integrated ν_μ and ν_e NC event rates are about one third of the corresponding CC event rates. In case of oscillation into a ν_τ, the rate of NC events is conserved. On the other hand, if oscillations occur into a sterile neutrino, the rate of upgoing ν_μ-NC is approximately reduced by a factor of two.

	$E_{min}(GeV)$	ν_μ	ν_e	ν_τ		
				10^{-2} eV^2	3×10^{-3} eV^2	10^{-3} eV^2
$\cos\theta < 0$	3.	14.73	5.04	1.29	1.06	0.62
	10.	4.56	1.06	0.95	0.71	0.27
	30.	1.32	0.21	0.40	0.17	0.03
$\cos\theta < -0.5$	3.	6.38	1.61	0.54	0.53	0.43
	10.	1.78	0.25	0.40	0.39	0.21
	30.	0.51	0.04	0.18	0.13	0.02

Table 3.1: Neutrino + anti-neutrino integrated CC event rate (kt·y)$^{-1}$ for $\cos(\theta) < 0$ and $\cos(\theta) < -0.5$. For the ν_τ case, rates for maximal mixing and three different values of Δm^2 are given. Rates for ν_μ and ν_e correspond to the no oscillation hypothesis.

These tables imply that high energy muon-less events must be selected. Moreover, in order to make the ν_τ appearance method effective, a detector of large mass is necessary, due to the small expected rate of ν_τ events, and with a good capability to discriminate muon-less events from the residual background of ν_μ and ν_e charged current interactions.

A high-density detector, optimised for the ν_μ disappearance method, fulfils most of these requirements: it guarantees a large mass and a reasonable rejection of events with penetrating tracks (muons), while the poor response of a coarse-grain calorimeter to electro-magnetic energy shifts the ν_e-CC interactions towards low visible energies, thus reducing the background of these events in the tau-appearance sample.

A detector with a relatively poor resolution to the hadronic energy could still be effective in the measurement of the up/down asymmetry of high energy muon-less events

integrated over a wide energy range (although the sensitivity could benefit from an improved resolution).

The main experimental challenge is represented by the detector capability of discriminating upgoing from downgoing muon-less events. This discrimination can be based on the analysis of the event topology and could also benefit from timing information.

These aspects will be further addressed in Chapter 5, where the analysis of the simulated data is presented.

Chapter 4

Experimental Setup

4.1 Introduction

In general, a detector capable to perform the measurements discussed in the previous chapter has to provide NC/CC discrimination, muon momentum and charge measurement, some hadronic energy reconstruction capability, up/down discrimination for muons above 1 GeV, and it has to provide an event sample with good L/E resolution, large enough to observe the modulation produced by ν_μ oscillations. Moreover, one requires a high rejection power against incoming stopping muons, better than 10^{-5} in the Gran Sasso underground laboratory. Finally the detector has to fit into an existing hall of the LNGS and it must have a reasonable cost.

All this can be achieved with a high-mass tracking detector with a coarse structure and magnetic field.

We shall mainly consider what we call the *baseline* option (figure 4.1). This is a detector consisting of a stack of 120 horizontal iron planes each 8 cm thick and with a surface area of 15×30 m^2, interleaved with planes of sensitive elements. The iron plates are magnetized at a magnetic induction exceeding 1 T. The total mass of the detector exceeds 34 kt. The sensitive elements provide two coordinates with a pitch of 3 cm, and a time resolution of 2 ns. Sensitive elements are housed in a 2 cm gap between the iron planes. The height of the detector is thus 12 metres.

A different option being considered has a similar structure as the baseline but with vertical planes. Such a configuration may offer interesting opportunities –which are being considered– in an operation with beams. It will be shown to provide similar reconstruction capabilities of the L/E pattern, but with some loss of efficiency around the vertical. This implies a loss of events at large L/E resulting in a somewhat reduced precision in the measurement of the mixing angle. The performance in the ν_τ/ν_s discrimination still has to be evaluated.

The final design will be defined after detailed studies and comparisons of performances, costs and construction times. The performance of the baseline option represents an important reference, since only configurations yielding at least a similar performance in the reconstruction of the L/E pattern will be considered for this experiment.

In this chapter we review the present status of the detector design.

For iron magnetization, extensive studies, which include power consumption and cost, have thus far been done for the baseline option only. As will be shown in the next

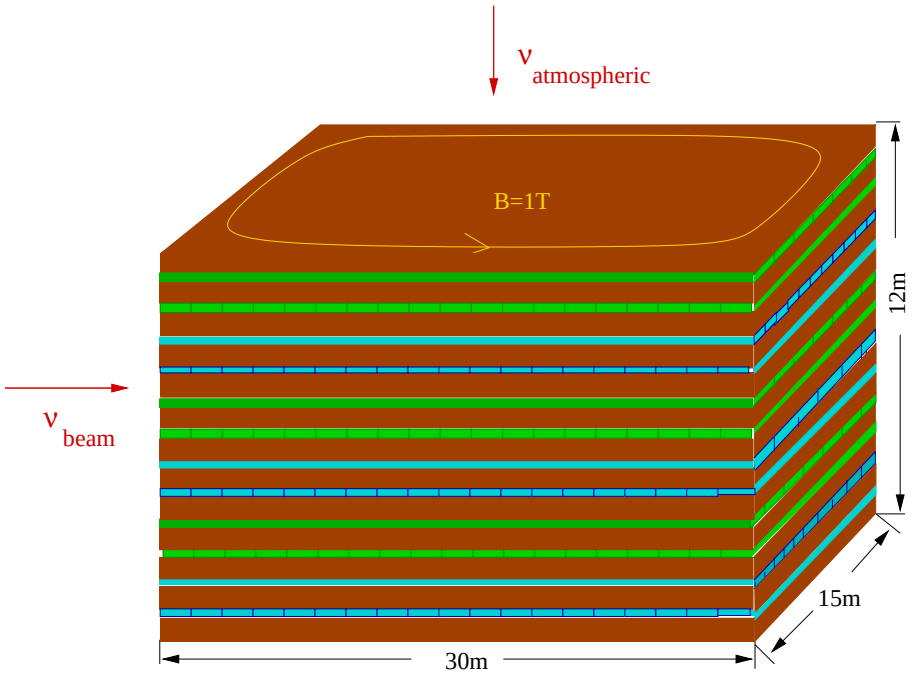

Figure 4.1: Baseline design of the magnetized calorimeter.

section, these studies indicate that a magnetic induction of about 1.2–1.4 T is affordable at reasonable cost and power consumption.

Two primary options are presently being considered as detector elements: Glass spark counters (resistive plate chambers), and scintillator bars with wave length shifter (WLS) read-out. Their performance, feasiblity and estimated cost will be discussed in the following sections and in Chapter 7.

As already mentioned, the baseline design is 30 m long, 15 m wide and 12 m high, which is consistent with construction and operation in the Gran Sasso Hall C. Other dimensions could be considered if necessary.

Finally, technical studies will be done in order to split the detector into two or three super-modules.

4.2 Magnetization of the iron plates

In the baseline option, the ideal magnetic field should be horizontal and uniform. However, to avoid huge power consumption and stray field, we have to contain the field lines strictly inside the iron. This requirement is of course conflicting with the ideal uniformity. We have found two possible layouts that are reasonable compromises between these requirements. We will call these layouts respectively layout H (the field lines lay in *horizontal* planes) and layout V (the field lines lay in *vertical* planes).

In the layout H, each field line lays entirely inside an individual iron plate. To obtain this, we need a *vertical* slot, crossing all the stack, through which the currents, generating the field, have to pass (see the Appendix A for more details).

In the layout V, the field lines run along each iron plate for almost all its length,

then they go into vertical paths (obtained filling with iron the ends of the slots, made for the detectors) and come back along another iron plate. In this layout, the currents generating the field cross the stack along its *horizontal* median plane, together with a layer of detectors (see the Appendix A for more details).

In the layout V, we call *end-caps* the regions containing the ends of the detector slots, filled with iron. They could be structured in vertical iron plates, interleaved with detectors, like the horizontal ones.

In the Appendix A we show that both the layouts allow to create a field of the order of $1.2 \div 1.4$ T, with a power consumption not exceeding 200 kW and a cost of the windings not exceeding 500 kEuro.

4.3 Glass Spark Counters

4.3.1 Basic structure and operation

As described in the previous chapter the baseline option for the experimental apparatus for atmospheric neutrino oscillation detection is a massive tracking calorimeter of about 34 kt of iron. A possible solution is a sampling calorimeter consisting of 120 8 cm thick iron slabs interleaved by detector planes. Taking into account the overall dimensions of the apparatus (30 m long, 15 m wide and 12 m high) the total detector surface is ~ 54000 m^2. The large active area requires a low cost detector, suitable for a fast mass production.

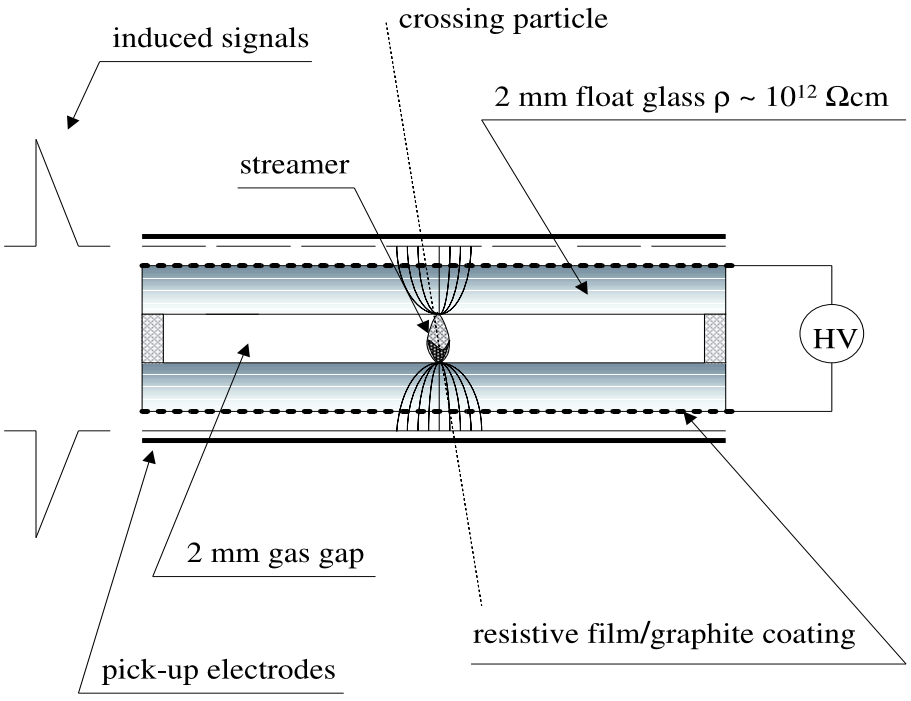

Figure 4.2: GSC: principle of operation.

For that reason we propose Glass Spark Counters (GSC) [40, 41, 42, 43, 44, 45, 46] as active elements, which provide a timing of the order of 1 ns, and therefore excellent up-down discrimination of muons from ν-interaction inside the apparatus.

The GSC (fig. 4.2) is a gaseous detector composed by two parallel electrodes made of glass with a volume resistivity of about 10^{12} Ωcm. The two electrodes, 2 mm thick, are kept 2 mm apart by means of suitable spacers. The gap between the two glass electrodes defines the gas volume where the particle detection occurs. Under particular gas mixture and electric field configurations (typically $\sim$48% Argon + $\sim$4% isobutane + $\sim$48% R134A and $\sim 4 \div 5$ kV/mm) the detector is operated in spark mode. Typical signal amplitudes of the order of $100 \div 200$ mV/50 Ω are observed, corresponding to a charge of about $100 \div 200$ pC (depending on the intensity of the applied electric field).

The use of highly resistive material as electrodes ensures that the spark discharges just a limited area around the spark location. The time to recover the electric field, depending on the electrode resistivity ($\tau \sim \rho\varepsilon$, where ρ is the glass volume resistivity and ε is its dielectric constant), avoids self-sustaining sparking.

The read-out of the detector is performed with external pick-up electrodes, allowing a bi-dimensional localization of the crossing particles together with its crossing time.

The details of the current GSC design and the proposed arrangement for the apparatus plane will be discussed in the next section.

4.3.2 GSC and apparatus design

A sketch of the GSC design is shown in fig. 4.3 [45]. It consists of a couple of float glass electrodes 1.75 m long, 25 cm wide and 2 mm thick. The 2 mm distance between the electrodes is ensured by NORYL spacers clamping the edges of the glass plates. These spacers sustain both electrodes, ensuring a gap tolerance at the level of a few microns, for uniform working conditions in a such large apparatus. The high voltage is applied to the electrodes by means of resistive adhesive film with a surface resistivity of about 200 kΩ/square. The detector is inserted into an extruded NORYL envelope, that ensures the gas containment. In such a way a possible variation of gas pressure does not change the distance between the electrodes. The HV connections to the resistive film are located in one of the two end caps that close the GSC module. External pick-up strips (not shown in fig. 4.3) are used to detect the induced pulses. All the materials used are commercially available, while the manpower is essentially due to film application on the glass surface and to the detector module assembling. This detector is conceived for the use in a underground laboratory. In fact all the materials are halogen free (PVC has been replaced by NORYL), the gas mixture is ecological and not flammable (Freon has been replaced by R134A, the isobutane percentage is well below the flammability level).

For the MONOLITH apparatus (fig. 4.4) the GSCs will be equipped with X-Y pick-up strip electrodes, both with a pitch of $\sim$ 3 cm, mounted on the opposite side of the detector planes. The pulses are induced on the strips and then discriminated by the electronics directly connected on the strip ends. The electronics should also provide a fast discriminated signal for timing purposes.

This type of readout system will provide a three-dimensional tracking of particles inside the apparatus with a time resolution of $\sim$ 1 ns and a spatial accuracy of $\sim$ 1 cm on both views.

In fig. 4.5 the GSC plane arrangement is shown. The detector plane insertion is along

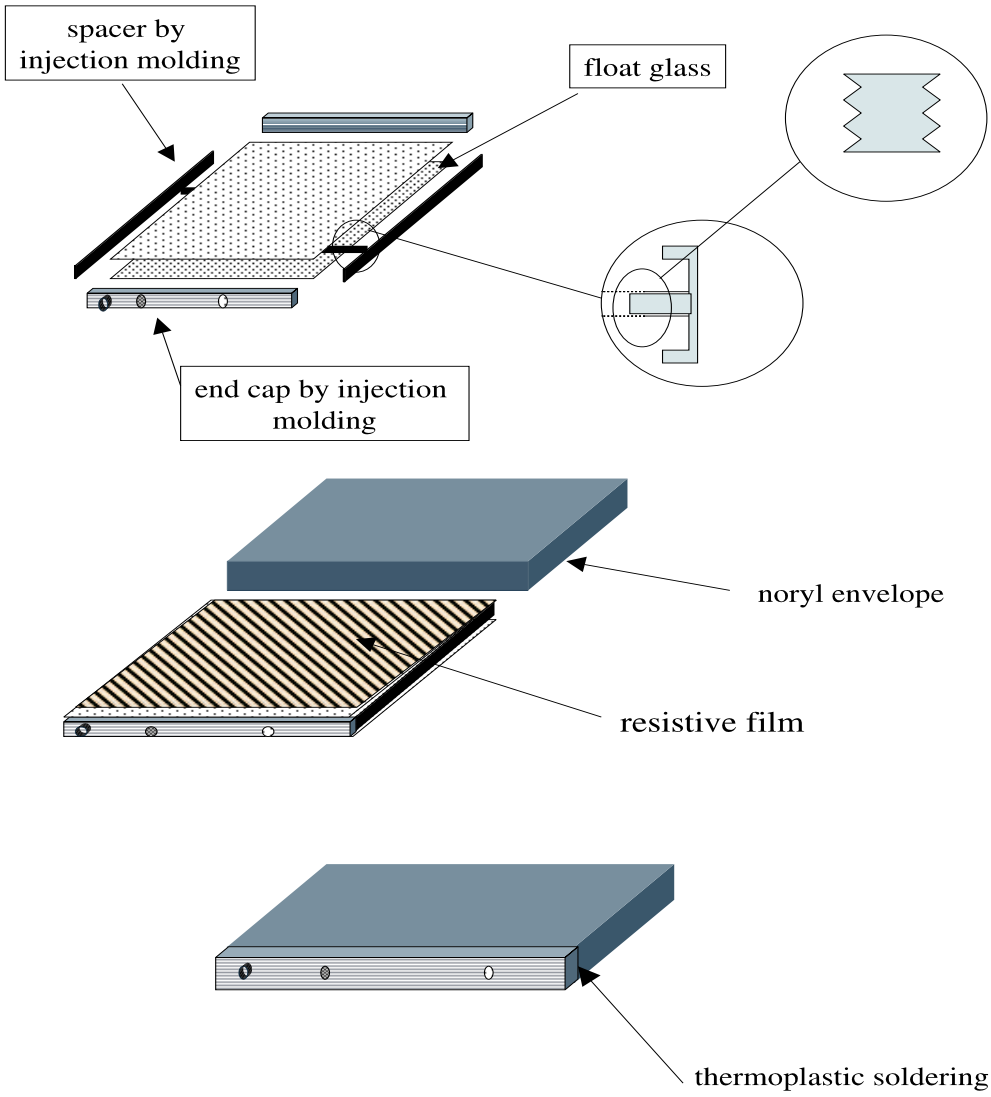

Figure 4.3: Schematic view of the GSC.

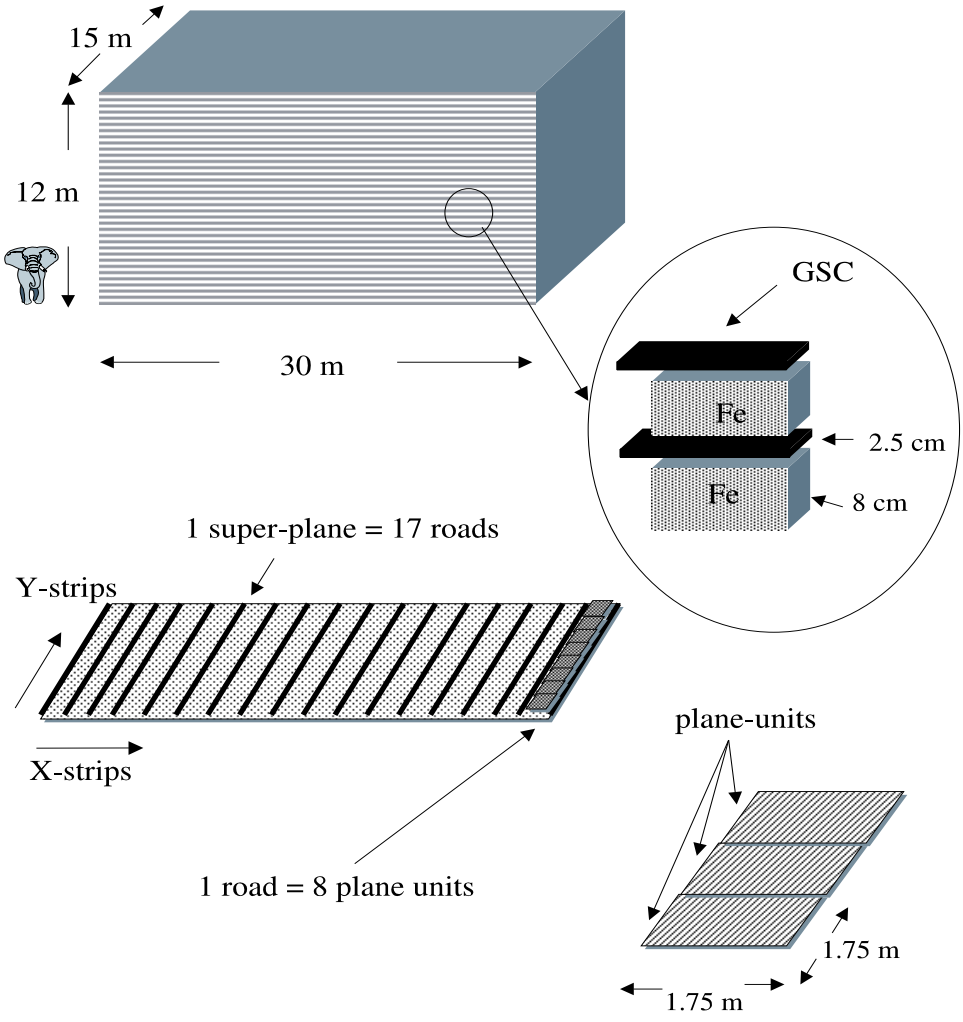

Figure 4.4: Schematic view of the MONOLITH apparatus.

the Y direction, as requested in the case of the so called *Layout V* magnet configuration (see section 4.2). The mechanical construction of the iron structure should not interfere

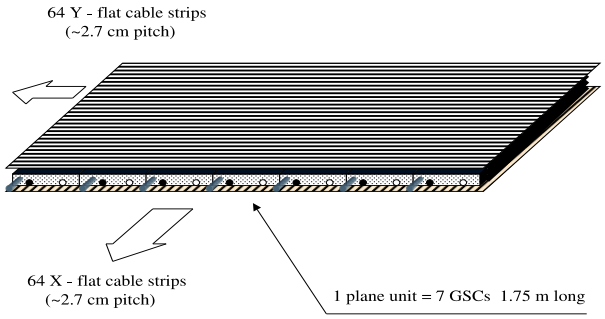

Figure 4.5: Schematic view of a GSC plane unit.

with the detector installation. The dimension of the underground hall permits a maximal length of the detector module of $\sim$ 1.75 m to allow module insertion. In this case, each detector *super-plane* is composed by 17 *roads*, 1.75 m wide and 15 m long, realized with 8 *plane units* 1.75 m long (fig. 4.4). To allow detector insertion after the assembly of the iron structure, each *plane unit* lies on a stiff aluminum support equipped as a trolley which can slide inside the iron gap. The *plane units* are rigidly attached to each other via the gas and HV connections. They are composed of 7 GSC detectors 0.25×1.75 m^2, equipped with X-Y strip planes (64 strips each, fig. 4.5). A scheme for multiplexing more strips into the same readout channel is being worked out. For instance, the X strips of each unit could be connected to those of the next unit to make 15 m long X strips along the *road* and then read out by digitizing electronics put on one strip end; the Y strips of each unit could be daisied into a chain (as illustrated in fig. 4.6) and then read out. Both X and Y front-end electronics are placed on the same detector side. In this scheme the second coordinate is fully determined only if the crossed plane unit is reconstructed. For this purpose both X and Y front end electronics should provide a fast discriminated output signal either for time measurement (the X one) or to solve the ambiguity on the Y cooordinate (the crossed plane unit is determined by the relative difference of the arrival time between the Y and X signal). Following this read-out scheme each *super-plane* would be read out with 2,176 X and Y digital channels and 34 fast discriminated signals, corresponding to 261,120 digital channels and only 4,080 TDC channels for the whole apparatus.

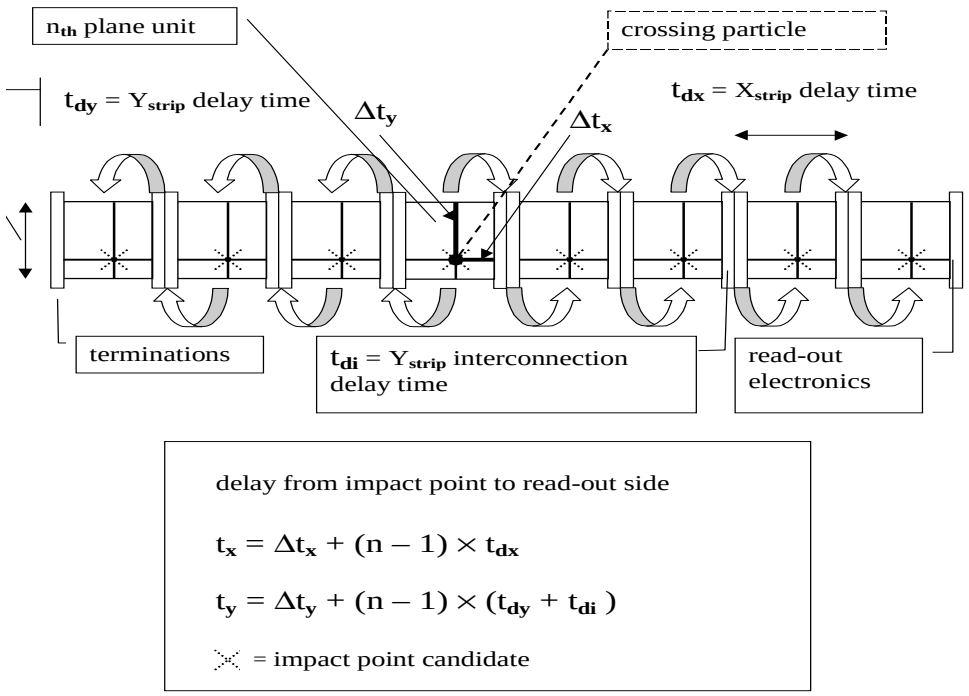

Figure 4.6: Particle impact point identification method.

4.3.3 Electronics and readout

According to the experiment requirements we have to identify crossing particles with $\sim$ 3 cm readout pitch and $\sim$2 ns timing resolution. Then signals coming out from strips have to be discriminated to obtain both spatial and timing information. Due to the huge number of readout channels involved it is too expensive to use high timing resolution discriminators for each strip. So, part of the signal (about 20%) is discriminated using low-cost, low-speed discriminators, while the rest of the signal is summed together with the respective ones coming from the other strips. The sum signal is discriminated using a high speed discriminator for timing information, as shown in fig. 4.7. The main

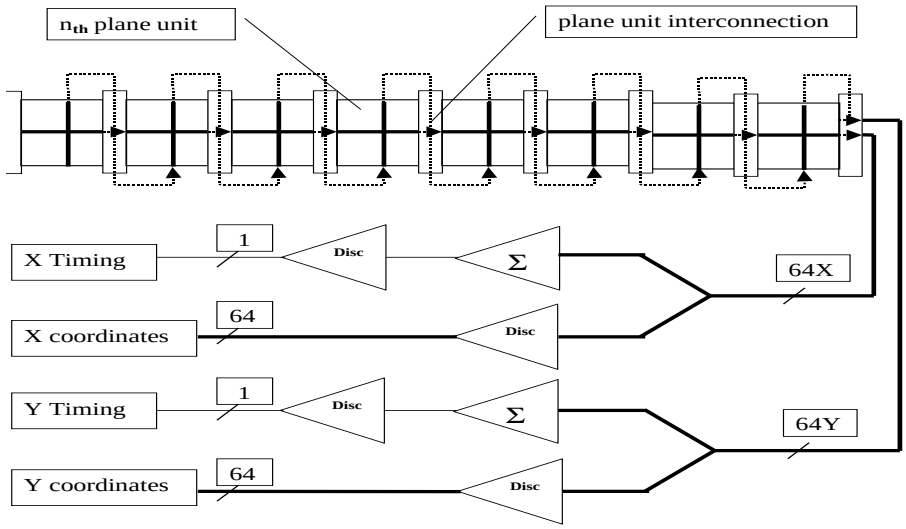

Figure 4.7: X and Y readout block diagram.

problem of the front end electronics comes from the inaccessibility of the Y view readout. A possible solution to overcome this problem is to integrate the Y view electronics into the detector itself. This arrangement allows the readout from a single side but has the following drawbacks:

- electronics reliability (it is almost impossible to replace broken electronics parts in the assembled detector);
- detector heating due to electronics power dissipation;

- huge number of Y readout channels (about 1 million channels for the whole apparatus);

A readout system overcoming the previous drawbacks is shown in fig. 4.6 . In the scheme each of the 64 Y strips of one plane unit is connected with the corresponding one of the following plane unit on the same road. This gives, for each road, a total number of 64 strips for the X view and 64 strips for the Y view (that is a reduction of a factor 8 in the number of Y strips readout channels). Because of the road Y strips interconnections, the X and Y information gives 8 possible couples of coordinates. To have the correct spatial information we have to look for the plane fired by the crossing particle. As shown in fig. 4.6, the identification of the plane unit is done by measuring the delay time between the Y and X views.

4.3.4 Detector performance

During last 10 years the performance, life-time and reliability of the GSC detector has been extensively studied by some of us. GSCs have been studied also by a group belonging to the BELLE experiment [46].

A set of measurements has been performed with a telescope made up of 4 horizontal planes [42]. A wide efficiency plateau has been obtained with a knee at 7.4 kV. The low noise operation of GSCs allows an easy monitoring and calibration of the device, by simply performing single counting rate measurements. A detector efficiency of 98% has been reached with a 25 cm wide chamber.

Using a scintillator telescope selecting cosmic ray muons, a GSC time resolution of about 480 ps has been measured with respect to a fast scintillator counter (with a measured time jitter of about 150 ps). The supplied voltage was 8.6 kV (about 1.2 kV above the knee) and the measurement lasted about 30 days.

Further detailed studies have been also performed on the glass properties [43], [44] and on the detector design optimization and engineering in order to make its construction easy and fast [45].

An 8 ton calorimeter prototype has been equipped at the LNGS by a group belonging to the MONOLITH collaboration. The prototype has been tested on the T7 PS beam facility at CERN to study the hadronic energy resolution and the reconstruction capability of the shower direction. The test module is made of 20 (1 m^2) iron slabs 5 cm thick (kindly borrowed from the ALEPH collaboration), interleaved by 21 GSC planes, for a total sensitive area of about 23 m^2. Each plane is equipped with 96 horizontal strips (1 cm pitch), equipped with digitizing front end electronics (SGS cards) on one end and with custom analog cards (realized at the LNGS) on the other end. The digital readout of the strips produces the event pattern, while the analog one provides the charge and time measurement of the event (for each plane). Fig. 4.8 shows an example of a 4 GeV test beam pion interacting in the 8 ton calorimeter prototype. Analysis of the data is in progress.

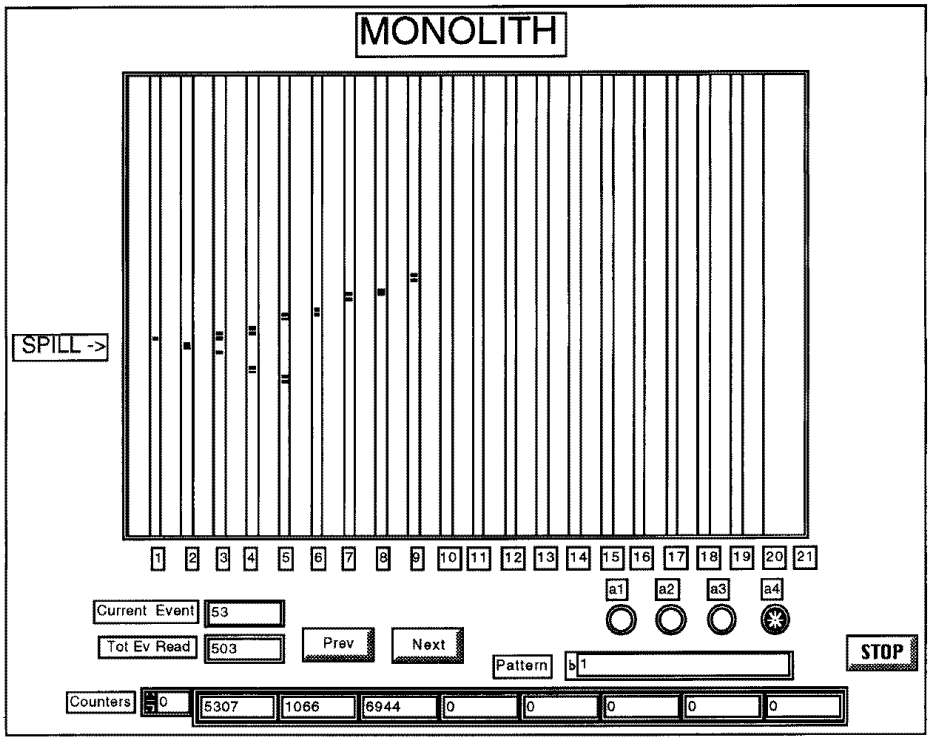

Figure 4.8: 4 GeV pion interacting in the 8 ton calorimeter prototype.

4.4 Scintillator Bars with WLS Fibres

4.4.1 Requirements

As an alternative active component we consider scintillator bars with wavelength-shifting (WLS) fibres and a highly integrated optoelectronic readout. This choice would allow to exploit the calorimetric properties of scintillators. The linear response at higher energies is expected to increase the resolution at lower L/E.

Detectors based on scintillators are widely applied for tracking and calorimetry. For dimensions up to 8 metres there is no doubt about a reliable performance. Scintillator bars with WLS fibres up to 12 metres have not been realized so far although they have been proposed [10, 14]. A careful optimization of the various parameters is required to meet the high requirements of the system:

- A high photon yield of the primary scintillator combined with good uniformity of photon emission along the bar.

- A high trapping efficiency of the WLS fibre and an efficient optical coupling of the fibre to the bar.

- To ensure a detectable light intensity after transport along the fibre of up to 12 metres, a long attenuation length is needed. Although five to six metre attenuation lengths are given in catalogs, batch to batch variations in reality can reach a factor of two difference in performance.

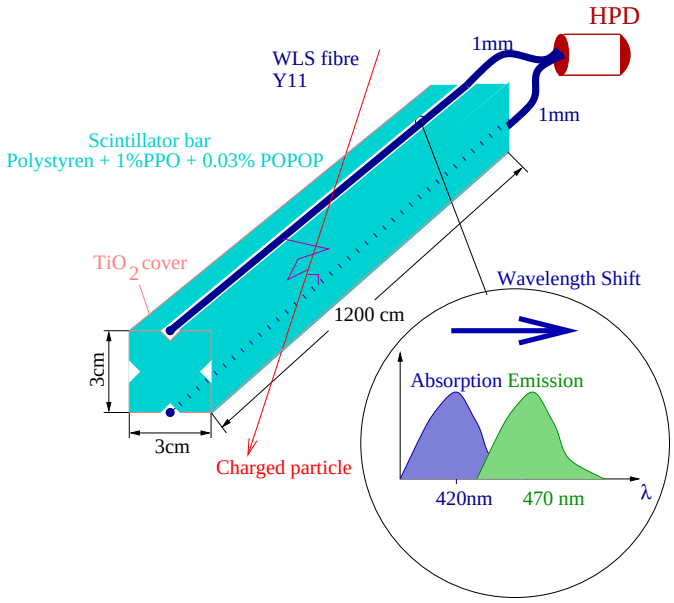

Figure 4.9: A module based on scintillator with WLS fibres. The fibres are read out on both ends by multichannel optoelectronic devices.

- To reduce self-absorption the created (blue) light should be shifted to a longer wavelength, typically around 500 nm.
- The spectral sensitivity of the photo-cathode should peak around the maximum of the emission spectrum. Not all manufacturers are able to fulfill this requirement.
- A good optical coupling between fibre and photo-cathode.
- An overall photoelectron yield sufficient to reach 2-3 ns time resolution.
- An efficient photon detection tube with a high integration level (large number of channels) to reduce the cost.
- Commercial availability of the components (bars, fibres, photo-tubes).
- Affordable cost for mass production of the scintillator bars.

4.4.2 The scintillator bar and fibre

The scintillator bars are made of polystyrene doped with 1% PPO and 0.03% POPOP, to ensure a high photon yield. Due to the large number of required bars we are considering extruded scintillator with a co-extruded TiO_2 layer for reflectivity, as proposed by MINOS [14]. On the surface, along the bar's axis, a groove will hold the WLS fibre. Important quality parameters are the uniformity of light emission along the bar and the surface quality to reduce reflection losses. They will be optimized during the R&D work, which has been started, with the manufacturers. Two companies have been contacted and are in principle able to fulfill our requirements.

Following the baseline design from Figure 4.1, we are considering bars between 12 and 15 metres length and a squared cross section of two by two cm. The final design will result from an optimization procedure based upon ongoing tests. The volume ratio of iron to scintillator will be around 4:1 reflecting the need of high mass and the financial constraint of the higher scintillator price.

Calculations of the light yield and first measurements indicate a marginally sufficient light yield with two fibres per bar. In view of the batch to batch variations of the fibre manufacturer and high accuracy of the calorimetric measurements we believe four fibres per bar, one on each side, are more reliable with only a small increase in total cost.

Fibres with acceptable light yield are commercially available and those found to have the best performance will be evaluated during ongoing tests. The baseline design features a double clad Kuraray fibre with the wavelength shifter Y11 and a diameter of 1 mm. We are investigating other fibre materials and larger diameters as well. Good optical contact of the fibre to the bar can be ensured by means of optical glue (e.g. Stycast or Bicron BC400).

The fibres from one bar are coupled to the same readout pad. They are read out on both ends resulting in a higher light yield and a spatial information along the bar.

We prefer a direct optical coupling of the WLS fibres to the photo-cathode. Fibres from neighbouring groups will be coupled to one tube to keep the additional length short. For 12 metre long bars, the maximal fibre length should not exceed 14 metres, therefore requiring the attenuation length to be five metre or better.

4.4.3 The read out

For the photon detector we see three possibilities:

A) Multi-channel Photomultiplier (PMT)

B) Hybrid Photodiode (HPD)

C) Electron Bombarded CCD (EBCCD)

All three were tested by the collaboration and show satisfactory results [47, 48, 49]. The EBCCD has the advantage of a very high level of multiplexing (only 1 readout per tube) and an excellent single photon detection efficiency [49], but no timing capabilities. Its single photon detection capability makes the HPD superior to the multi-anode PMT. The peaks for each photo-electron are well separated due to low gain fluctuations of the HPD and a detection threshold at one photo-electron will not cause light losses. Figure 4.10 shows the light yield measured with an HPD from DEP. A 61-channel HPD is commercially available, with an individual pixel size of 2 mm^2 and a very good pixel-to-pixel gain uniformity. Larger pixels are available when the number of pixels per tube is reduced. Every pixel has an individual feed-through which contributes to the fast response of the HPD (in contrast to the EBCCD) but makes the number of readout channels identical to the number of bars, 4×10^4. Housing a much larger number of pixels in a single HPD tube is another possibility [50].

Because of their capability of single photon detection, gain uniformity, and fast timing we opt for HPD's as a baseline design. The other options are being followed up within our collaboration.

An important question is the timing performance of a scintillator system. The short transfer time of the read out devices (HPD, PMT), of a few nanoseconds, would allow a

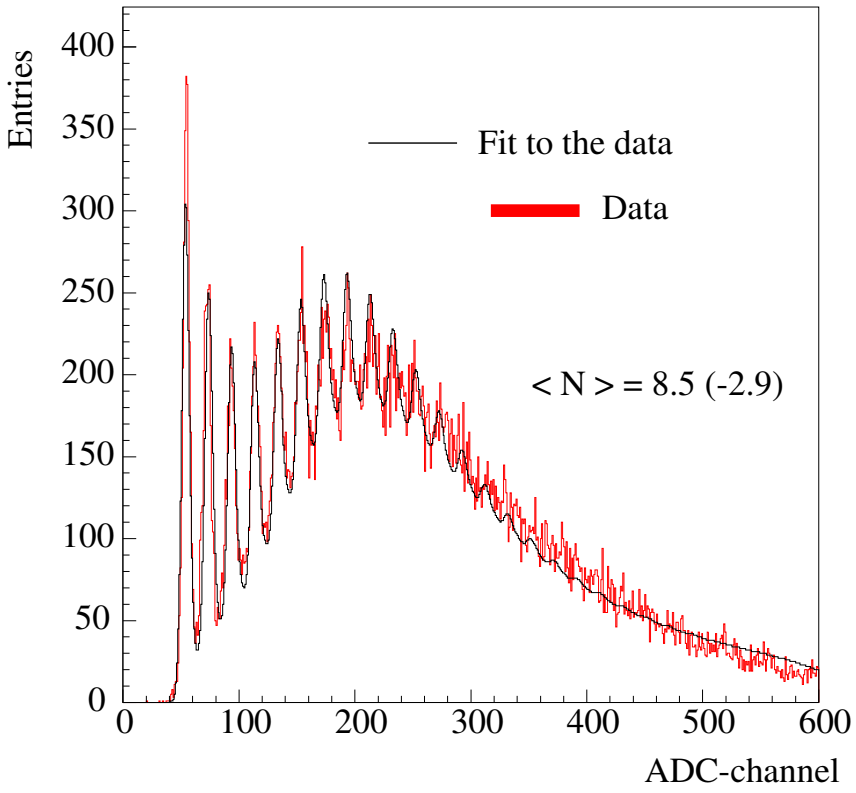

Figure 4.10: Measured light yield with a scintillating bundle of 1×1 mm^2 cross section. Emerging photons were detected by a single-channel HPD [51].

good time resolution. However, the decay time of the scintillator is rather slow ($\tau \approx 7$ ns) if a high light yield is required. The dispersion of light transmission can be calculated from the condition of total reflections. For a typical double clad fibre the variations in the arrival time of photons are $\pm$ 2.5 ns and can be considered negligible with respect to the statistical fluctuations of the light decay. The effect of the electronics noise on the time resolution is expected to be less than 4 ns even for low light yields due to the low gain fluctuations.

For a reliable estimate of the timing performance, the decay time of different scintillators with fibres was measured and used as an input for a Monte-Carlo simulation including electronic noise. First results indicate that a time resolution of 3 ns is possible if the mean number of detected photo-electrons is 10, despite a measured effective decay time of 10 ns.

4.5 General Infrastructure

Since the detector has not yet been finalised, detailed studies of the infrastructure requirements still have to be worked out. Here, we present some general considerations.

The difficulty of the work inside the cavern and the necessity to minimise the construction phase ($\sim$3 years) impose a certain number of constraints:

- detector construction and assembling outside the cavern
- iron modularity compatible with earthquake safety rules
- a suitable optimisation of the apparatus assembly

The preferred hall is Hall C: given the total mass of the detector (fixed by the number of events necessary) the larger transverse dimension results in a better containment of the neutrino events, or, in other words, a larger fiducial volume. The maximal width for a detector is about 15 m, given the hall width of 18 m. It is mandatory to keep the first 12 m of the hall free to permit entering of lorries. The use of hall B is also considered to be possible. The reduction in the transverse dimension can be recovered by increasing the length from 30 m to 50 m. The length of the detectors would be shorter with a potential benefit in performance.

The maximum dimension of a single piece with which to assemble the detector is determined by the lorry dimensions (typically $12 \times 2.5\ m^2$) and the crane capability. For a fast assembly one could, for instance, imagine to transport four parts of an iron layer of $7.5 \times 1.0 \times 0.08$ m^3 or $3.75 \times 1.8 \times 0.08$ m^3. Horizontal planes can be assembled by placing these parts side by side and welding them together to form a well linked structure including spaces for the active detector planes. A similar procedure can be used for vertical planes: in this case it is necessary to add some special supports when starting the assembly until the structure becomes self-supporting. These procedures remain valid for sheet thicknesses down to 4 cm.

As a first step, the iron could be installed layer by layer and, later, be filled with the active detectors. In such a scheme, the sensitive detectors are constructed with a high modularity in order to decouple detector assembly and installation. The maximum length of a module is linked to the available space of 1.5 metres on both sides of the detector.

The LNGS is located in a seismic region requiring the structure to resist to an horizontal acceleration of 0.2 g. A possible solution is to link all the sheets one to the other by welding. The number and the lenght of the welding points must be calculated carefully. On a smaller structure (8×8 m^2) calculations show that the goal can be achieved with an adequate number of welding points.

Chapter 5

Analysis and Performance

5.1 Introduction

In this Chapter, results obtained from a full simulation of the experiment are presented. The analysis of simulated data has been performed in the framework of the experimental methods outlined in Chapter 3. Only the capabilities of the ν_μ disappearance and of the ν_τ appearance techniques have been fully evaluated and are reported hereafter in sections 5.3 and 5.4. The first technique, based on the comparison of upward and downward going events with a high-energy muon, will test the hypothesis of ν_μ oscillations and measure the oscillation parameters; the second technique, which relies on the comparison of rates of upward and downward muon-less events of high energy, will be used to discriminate between oscillations into a sterile or a τ neutrino.

Neutrino interactions in iron have been generated by G. Battistoni and P. Lipari: the differential distribution of the atmospheric neutrino fluxes at Gran Sasso is described by the Bartol model [52]; neutrino interactions are calculated with GRV94 parton distributions [53] with explicit inclusion of the contribution of quasi-elastic scattering and of single pion production to the neutrino cross-sections [54]. The GEANT package [55] has been used for the detector simulation.

In the experiment simulation, a detector consisting of a stack of 120 horizontal iron planes 8 cm thick and 15×30 m^2 surface, interleaved by planes of sensitive elements, has been considered. The sensitive elements for tracking and timing have been assumed to be housed in a 2 cm gap between the iron planes and provide two coordinate readout with a pitch of 3 cm and a 2 ns timing resolution. The detector has a total mass exceeding 34 kt. A magnetic induction of toroidal shape of 1 T has been assumed in horizontal planes.

Alternative geometries, with vertical iron planes, have also been simulated. In section 5.5, preliminary results obtained with this configuration are discussed.

5.2 Muon and hadronic shower reconstruction

At the reconstruction stage, the muon direction is obtained by a best fit procedure to the muon track, which accounts for effects of detector resolution, multiple scattering, energy loss along the track and magnetic field. Optimisation of the track-fitting procedure is still in progress.

The muon energy is mainly determined by range for stopping muons and by track

curvature for outgoing muons. The energy resolution on the sample of stopping muons produced by ν_μ-CC interaction is on average better than 6%, with the sole quality request that the muon track span at least seven layers. With the same request, the average resolution on outgoing muons is $\sigma(1/p)/(1/p) \simeq 22\%$; the additional request – explained in the next section – that the track length inside the calorimeter be larger than 4 m brings the average momentum resolution to about 15%, essentially limited by multiple scattering in iron. An improved resolution is achieved at higher field intensity. The dependence of the momentum resolution on the track length, the pitch angle to the field and the magnetic induction has been found to agree with expectations.

From the analysis of the track curvature, the identification of the muon charge is possible. Due to the field configuration the charge identification is best achieved near the vertical direction, perpendicular to the field lines. On average 85% of the muons with a track length of at least seven layers have their charge correctly assigned, with an identification capability varying from 75% near the horizontal to 90% along the vertical direction (perpendicular to the field). For very long tracks, as they occur for upward throughgoing muons (typically about 12 m) charge discrimination is better, and momenta can be measured up to several hundred GeV.

The direction of the muon at the vertex, from which the neutrino direction is estimated, is reconstructed with an average resolution of about 10 mrad. This has a negligible effect on the resolution on the neutrino direction, which is limited by the μ-ν scattering angle.

The hadronic energy is estimated from the hit multiplicity in the calorimeter (digital information). The detector has a coarse hadronic energy resolution and a poor capability of reconstructing the hadronic energy flow. According to the simulation the dependence of the energy resolution on the hadronic energy can be parametrised as $\sigma(E)/E = 90\%/\sqrt{E\ (\mathrm{GeV})} \oplus 30\%$, averaged over all shower directions. As explained by equation (3.2) of Chapter 3 and discussed in the next section, the overall resolution on the neutrino energy, which enters in the measurement of the L/E and is generally dominated by the fluctuations in the hadronic shower, can be controlled by proper selection criteria, related to the in-elasticity of the event.

5.3 Disappearance of muon neutrinos

Oscillation parameters are not known *a priori*, therefore a unique set of event selections and a unique analysis method have been defined in order to make the oscillation pattern detectable for every possible experimental outcome.

In order to select a pure ν_μ charged current sample, only events with a reconstructed track corresponding to a muon of at least 1.5 GeV are retained in the analysis. This energy cut also ensures a good up/down symmetry in the absence of oscillations. In order to reject – in a real experiment – the background due to incoming cosmic ray muons, a further selection requires the events to be either fully contained in a fiducial volume corresponding to about 85% of the detector, or to have a single outgoing track (muon) with a reconstructed range greater than 4 metres; in both samples the muon is required to hit at least seven layers. For the partially contained events, the requirement of a track length of 4 m corresponds to an up/down separation of about 10^{-6} for 2 ns timing resolution, which should be sufficient to guarantee the rejection of the residual cosmic muon background in the Gran Sasso laboratory. The observation of hadronic activity at the event vertex

and the analysis of the track curvature could provide further discrimination capability between incoming muons and neutrino interactions.

Further selections, based on the quality of the muon track fit, and on event kinematics, are then applied in order to guarantee that the final sample has the required L/E resolution (better than 50% Full Width Half Maximum (FWHM)) over the whole L/E range. These selections have been tuned according to the discussion given in Chapter 3 (see equations 3.1 and 3.2) and essentially consist in a tight requirement on the estimated precision in the reconstruction of the incoming neutrino direction. At low muon energies only events of small in-elasticity and far from the horizontal are retained, while for large muon energies deep-inelastic events even rather near to the horizontal can be selected. For contained events, and given the detector characteristics, this is achieved by requiring $y \tan^2 \theta_\nu < 0.75 E_\nu$, where $y = E_h/E_\nu$, θ_ν and E_ν are the interaction in-elasticity, the zenith angle and the energy of the neutrino. For outgoing muons, since this sample is populated by events of relatively high energy, the only requirement is that the energy of the muon be estimated from the track fit with an error smaller than 30%. The L/E resolution on the events surviving these selections is shown in figure 5.1.

Altogether, these selections reduce the charged-current interaction rate of "unoscillated" downward muon neutrinos to about 7 per kty (20% of the total rate of muon neutrinos above 1 GeV). The presence of a magnetic field, which allows to include events with an outgoing muon, increases the acceptance for L/E less than 300 km/GeV by a factor 2. This is best seen from figure 5.2, which shows the efficiency of the selections as a function of the muon angle and of L/E.

The purity of the ν_μ-CC sample selected is around 99%.

By taking advantage of the timing capabilities of the sensitive detectors (2 ns), the flight direction is determined in each event from a least-square fit of the timing in each layer versus the layer number. Negative (positive) time-of-flight differences indicate downgoing (upgoing) events. No attempt to filter hits not belonging to the muon track has been made, nor has the identification of the event vertex from the hadronic activity been tried yet. The up/down discrimination of this method is about 95%, the residual confusion being due either to very horizontal events in which the muon produced in the neutrino scattering is in the opposite hemisphere with respect to the incoming neutrino or, more importantly, to almost horizontal events in which the muon track has a vertical extension comparable to the one of the hadronic shower. These latter events are easily resolved by hand scanning. Advances in pattern recognition will probably achieve this by automatic means. If not, the event sample is relatively small and it can be done by hand scanning. In the following a perfect up/down discrimination is assumed.

Data have been generated for several different values of oscillation parameters and the analysis of the L/E spectra obtained by applying the outlined selections has been based on a binned maximum-likelihood procedure. Similarly to the definition of event selections, the bin boundaries of the L/E distributions have been fixed without prior knowledge of the oscillation parameters. An equal bin-size on a logarithmic scale, corresponding to a constant relative L/E resolution, has been adopted. It can be shown that, in order to keep sensitivity to the oscillation pattern for every possible (yet unknown) value of Δm^2, the bin-size should satisfy $\Delta \log(L/E) \leq 0.5$ [56]. As for the requirement of an L/E resolution better than 50% FWHM, the upper limit at 0.5 on the bin-size is set by the requirement that the oscillation be sampled at twice its frequency at least over the first modulation period.

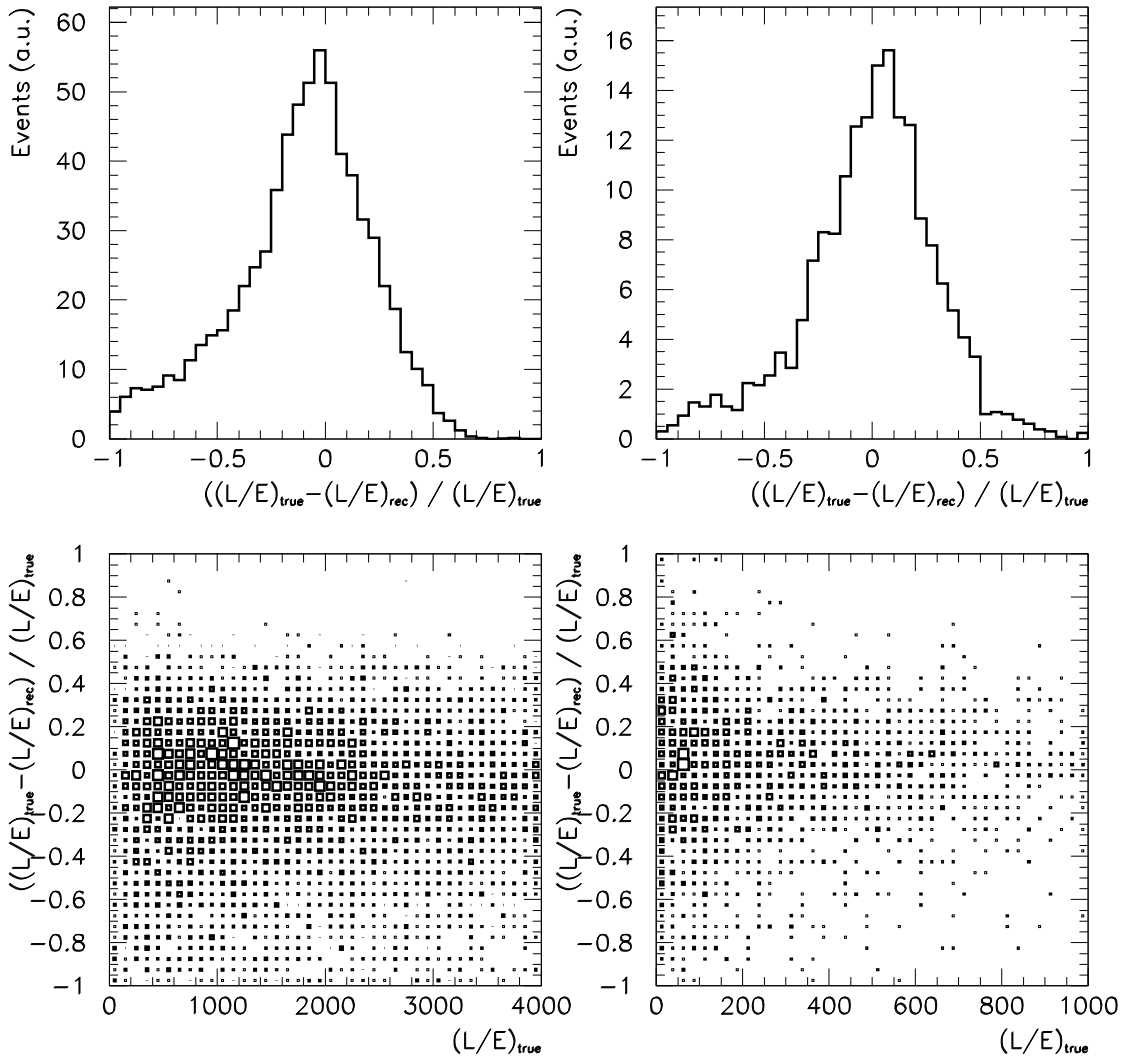

Figure 5.1: L/E resolution for contained (left) and partially contained (right) events after the selections discussed in the text.

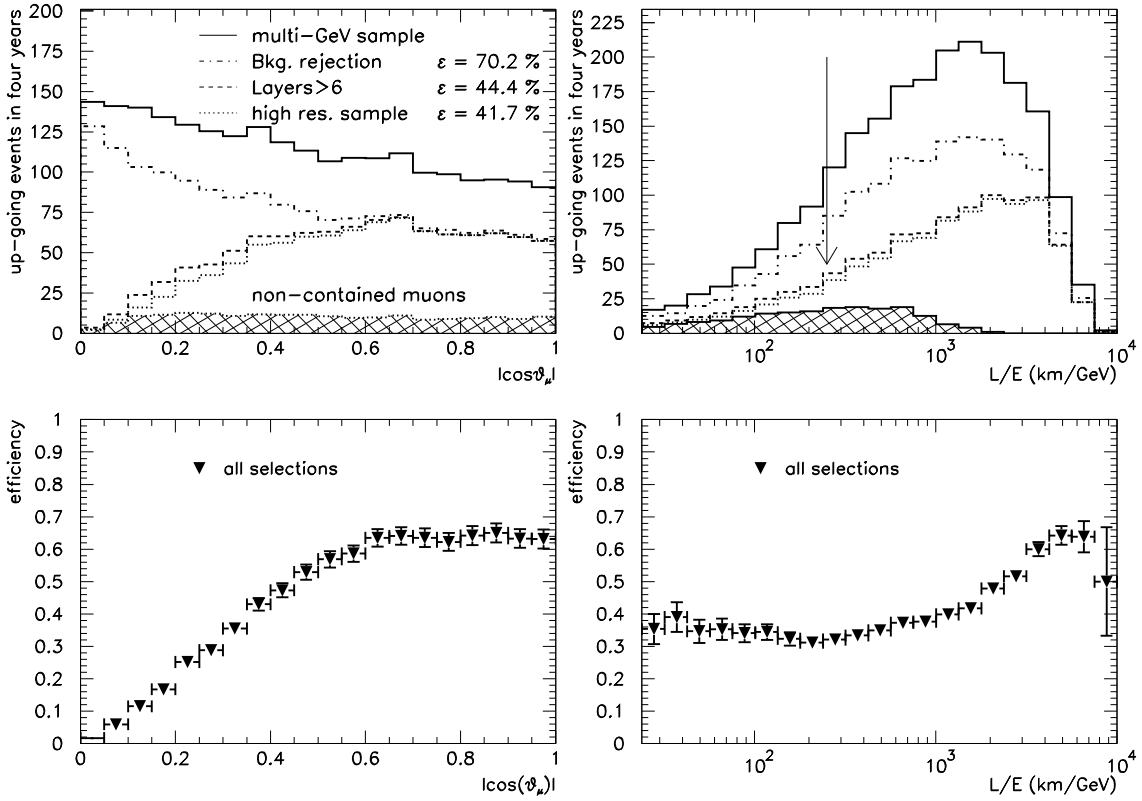

Figure 5.2: Effects of the selections described in the text on a reference sample of ν_μ–CC interactions with a final state muon of energy larger than 1.5 GeV ("multi-GeV sample"). The $\cos\theta_\mu$ and the L/E distribution for upgoing neutrinos as well as the selection efficiencies are shown. The hatched area represents the contribution to the selected sample of partially contained events. For $\Delta m^2 = 3.5 \times 10^{-3}$ eV^2, the present best-fit value of Super-Kamiokande [24], the first oscillation minimum would be located at $L/E \sim 250$ km/GeV, indicated by the arrow.

The likelihood function compares the observed rates of upgoing to downgoing events as a function of L/E and is defined as:

$$\mathcal{L} = \prod_{i=1}^{N_{bins}} \int_0^\infty \frac{\mu_i^{D_i} e^{-\mu_i}}{D_i!} \left[\mu_i P_i(\Theta, \Delta m^2)\right]^{U_i} \frac{\exp\left[-\mu_i P_i(\Theta, \Delta m^2)\right]}{U_i!} d\mu_i, \tag{5.1}$$

where the first term accounts for the Poisson probability that an expectation value of μ_i events would have produced the D_i downgoing events actually observed, while the second term gives the Poisson probability to observe U_i upgoing events when $\mu_i P_i(\Theta, \Delta m^2)$ are expected. $P_i(\Theta, \Delta m^2)$ represent the ν_μ survival probability for the i-th bin for given values of oscillation parameters and is parametrised as:

$$P(L/E; \Theta, \Delta m^2) = 1 - \frac{\sin^2(2\Theta)}{2}\left[1 - R(\Delta m^2, L/E)\cos(2.54\Delta m^2 L/E)\right], \tag{5.2}$$

where $R(\Delta m^2, L/E)$ folds in the experimental resolution and is taken as the Fourier transform of the resolution function of Fig. 5.1. This parametrisation of the survival probability is valid under the assumption that the L/E resolution function be symmetric and that the L/E spectra of upgoing and downgoing neutrinos be (practically) flat [57]. Both these assumptions are reasonably satisfied. In particular, in the region where the first oscillation would manifest itself for any value of Δm^2 allowed by the Super-Kamiokande results, the L/E spectrum of selected events exhibits a variation of order 10% over a range where the resolution function changes by a factor 2. Studies on systematic effects related to the knowledge of the resolution function are in progress.

The L/E distributions obtained with the outlined selections are shown in Fig. 5.3 and Fig. 5.4 for Δm^2 ranging from 7×10^{-4} to 8×10^{-3} eV^2 and maximal mixing. The figures also show the discovery potential (allowed regions of the oscillation parameter space) of the experiment after four years of exposure as determined from the outlined fitting procedure.

For large values of Δm^2 this approach loses sensitivity to the determination of oscillation frequency, because of the limited statistics at small L/E. At Δm^2 around 10^{-2} eV^2 oscillation starts to manifest in the downgoing sample and the Picchi & Pietropaolo's method adopted here is not optimal. Still an up/down asymmetry will be clearly visible. Moreover, for Δm^2 larger than a few 10^{-2} eV^2, upward neutrinos – at large L/E – will be in complete oscillation, while the oscillation pattern would become detectable in the downward sample. In this limit, a mirror distance $L'(\theta) = L(\pi - \theta)$ can be assigned to upward neutrinos, which can be used as a reference L/E distribution for downward neutrinos. In this case, due to the uncertain estimate of the neutrino path-length for downgoing neutrinos related to our ignorance of their production height in the atmosphere, there would be some model dependence in the determination of oscillation parameters. Nonetheless, the observation of an oscillation pattern would still firmly test the oscillation hypothesis. An example of the L/E distribution and results obtained with this analysis are shown in Fig. 5.5.

The results of the outlined analysis are summarised in figure 5.6. The precision on oscillation parameters (allowed regions at 90% C.L.) that can be achieved in four years of exposure is compared to the regions at 90% C.L. allowed by the Kamiokande and Super-Kamiokande results. In the absence of oscillations, the arguments presented can be used to exclude a region of oscillation parameters. The exclusion limits that this experiment

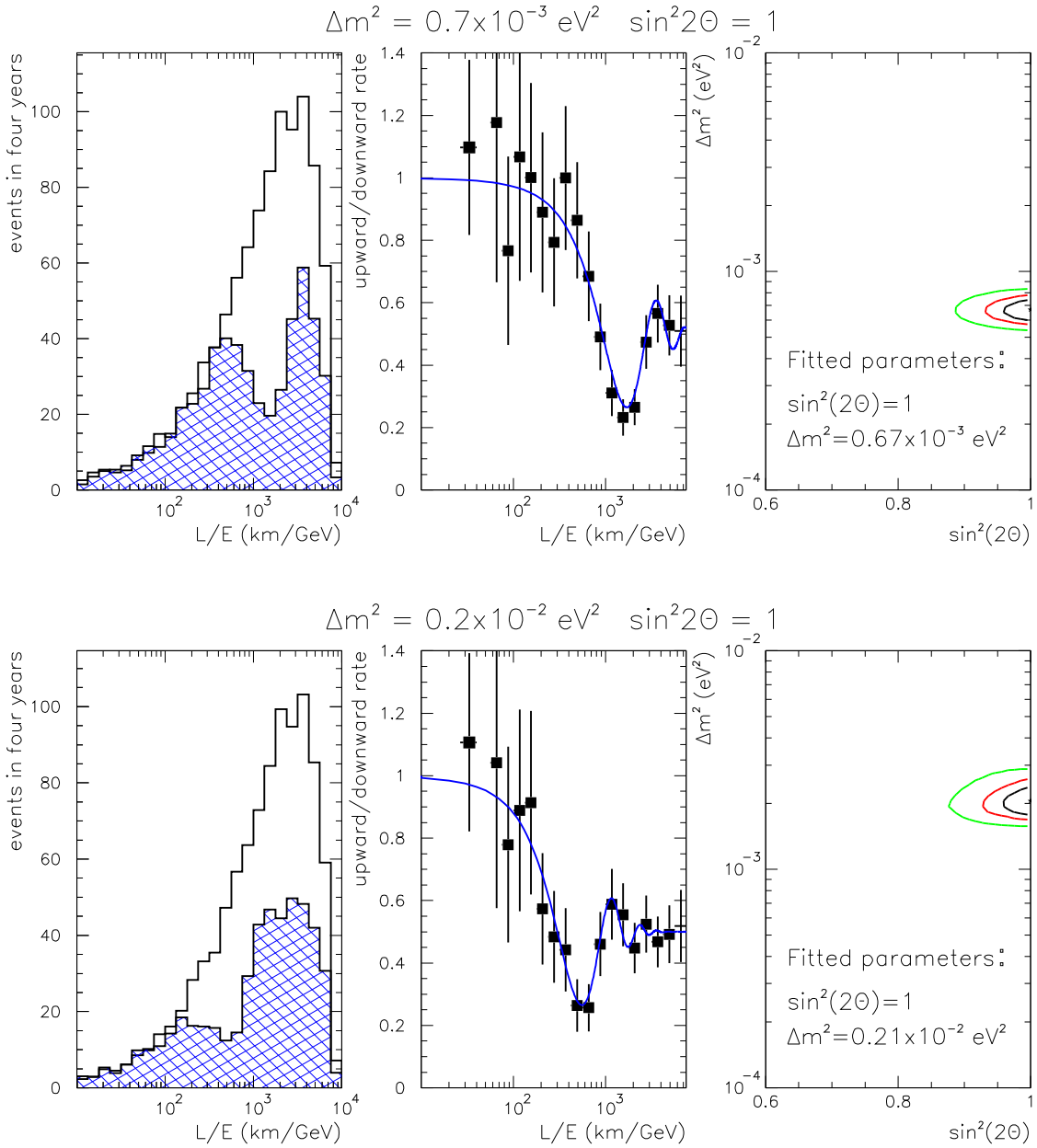

Figure 5.3: Results of the L/E analysis on a simulated sample in the presence of $\nu_\mu \to \nu_x$ oscillations, with parameters $\Delta m^2 = 7 \times 10^{-4}$ eV^2 and $\sin^2(2\Theta) = 1.0$ (top) and $\Delta m^2 = 2 \times 10^{-3}$ eV^2 and $\sin^2(2\Theta) = 1.0$. The figures show from left to right: L/E spectra for upward muon events (hatched area) and downward ones (open area); their ratio with the best-fit superimposed (the first point is integrated over the first six bins) and the result of the fit with the corresponding allowed regions for oscillation parameters at 68%, 90% and 99% C.L.. Simulated statistics correspond to 25 years of data taking, rate normalisation, error bars and errors entering in the best fit procedure correspond to 4 years. It has been checked that this procedure yields a good approximation of the exact sensitivity contours.

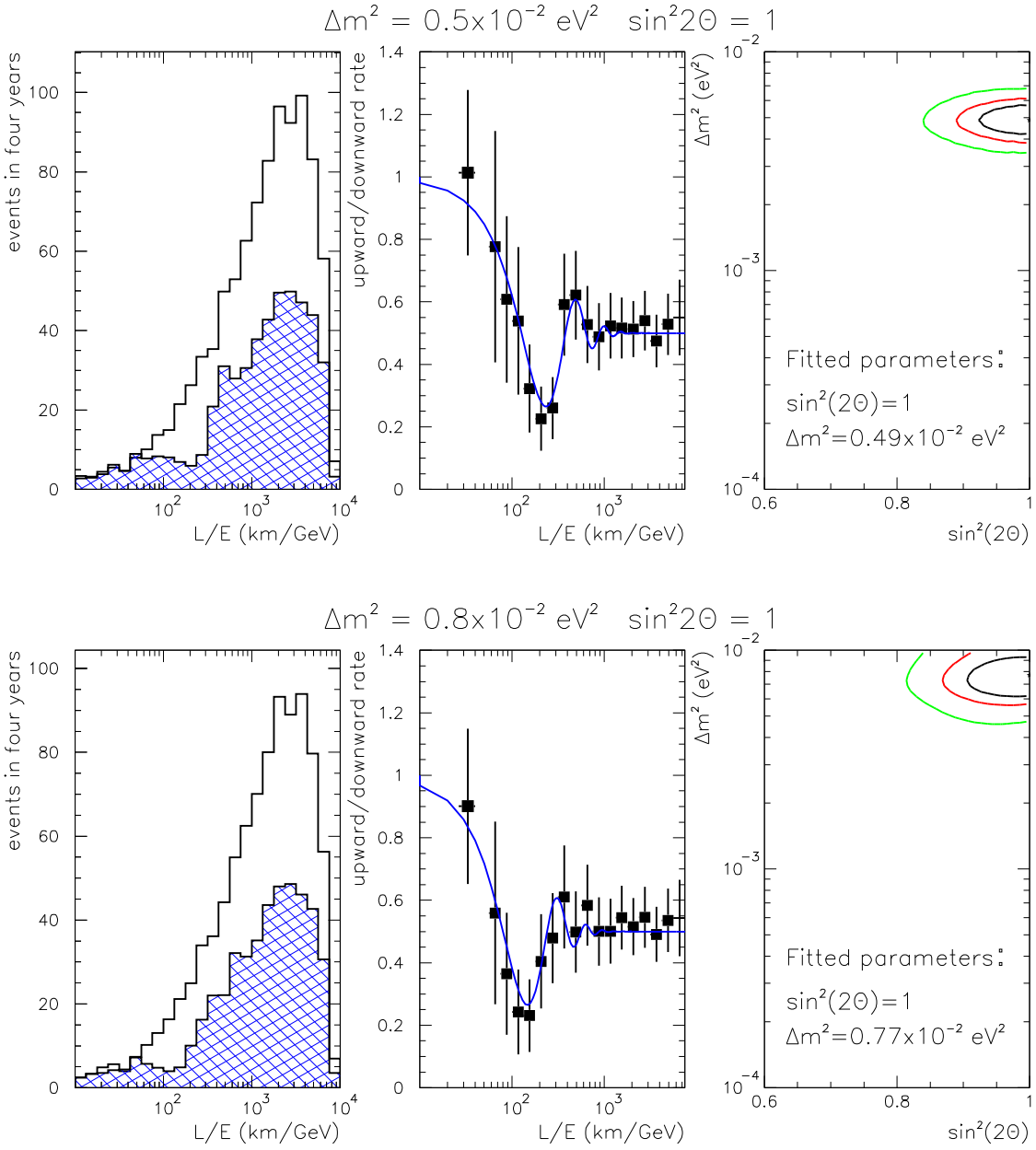

Figure 5.4: As Fig. 5.3, for $\Delta m^2 = 5 \times 10^{-3}$ eV^2 and $\sin^2(2\Theta) = 1$ (top) and $\Delta m^2 = 8 \times 10^{-3}$ eV^2 and $\sin^2(2\Theta) = 1$ (bottom).

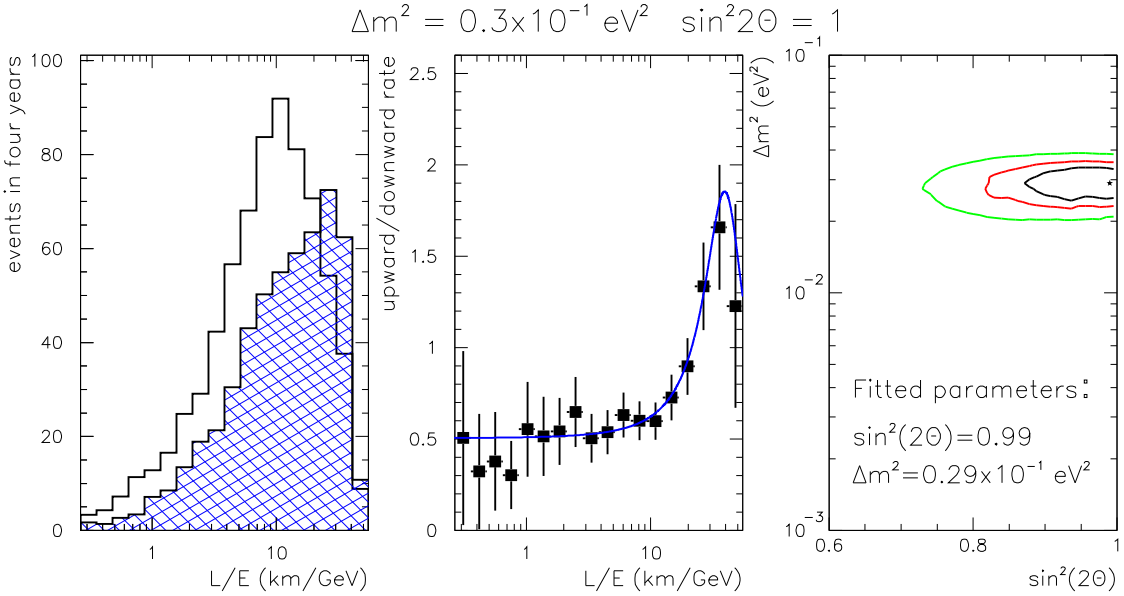

Figure 5.5: As Fig. 5.3, for $\Delta m^2 = 3 \times 10^{-2}$ eV^2 and $\sin^2(2\Theta) = 1$. As explained in the text, an *inverse* oscillation pattern appears for large values of Δm^2.

will be able to set after an exposure of one year at 99% C.L. or 4 years at 90% and 99% C.L. are also shown in the figure.

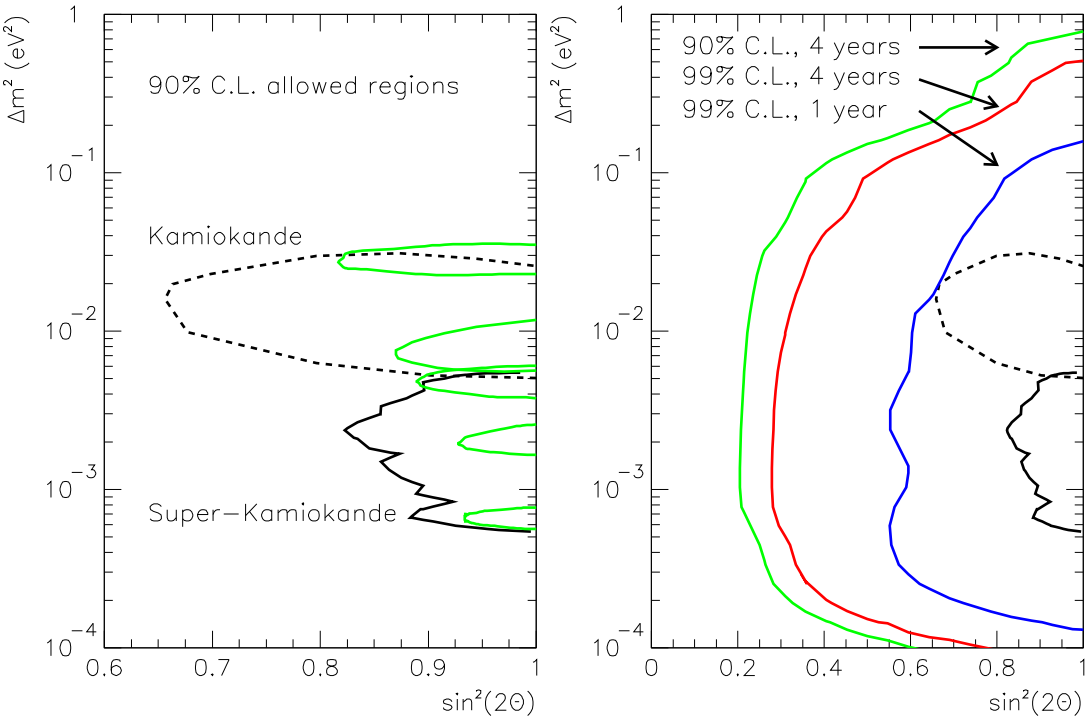

Figure 5.6: *Left*: Expected allowed regions of $\nu_\mu - \nu_\tau$ oscillation parameters for MONOLITH after four years of exposure, as obtained by the analysis described in the text: the results of the simulation for $\Delta m^2 = 0.7, 2, 5, 8, 30 \times 10^{-3}$ eV^2 and maximal mixing are shown. *Right*: MONOLITH exclusion curves at 90% and 99% C.L. after one or 4 years of data taking assuming no oscillations. The full (dashed) black line shows the published results of the Super-Kamiokande [3] (Kamiokande [16]) experiment.

5.4 Appearance of tau neutrinos

If evidence of ν_μ disappearance is observed, for $\Delta m^2 > 3 \times 10^{-3}$ eV^2, the appearance of τ neutrino charged-current interactions can be searched for to distinguish between $\nu_\mu \to \nu_\tau$ and $\nu_\mu \to \nu_s$ oscillations. As discussed in Section 2, this method consists in measuring the upward/downward ratio of muon-less events, as a function of the visible energy. Charged-current ν_τ interactions would in fact result in an excess of muon-less events in the upward sample at high energies, due to the large τ branching ratio into muon-less channels ($BR \simeq 0.8$). Moreover, because of threshold effect on τ production, events of large visible energy must be selected, in order to enhance the relative ν_τ contribution to the muon-less event sample.

This method was first considered in [9], where the selection of muon-less candidates (defined as events without non-interacting tracks longer than 1 m, equivalent to a m.i.p. of 0.9 GeV) and the up/down discrimination were largely based on hand scanning. Since the statistics of these events is not large, hand scanning is affordable. Here, however, results of an automated analysis are reported.

The selection of muon-less events is based on the ratio of the visible energy to the event length and on the recognition of a penetrating track, defined as muon candidate of energy greater than 1.5 GeV (taken from simulation truth). The sample of muon-less candidates selected by these criteria has a slightly larger contamination of ν_μ-CC events than the muon-less sample of Ref. [9]. However, the comparison of visible energy and event length does not require pattern recognition, while hand scanning shows that muons of 1.5 GeV are easily visible and within the reach of further progress in pattern recognition algorithms.

In addition, in order to achieve good up/down discrimination, events with limited vertical development have been rejected by requiring that at least 5 layers be fired and that the visible energy in the event obtained from the hit multiplicity be larger than 4 GeV.

These selections have an efficiency on ν_τ interactions followed by muon-less τ decays of about 60%, while the purity of the upgoing muon-less sample, assuming perfect up/down discrimination, is about 25%. The ν_μ-CC and ν_e-CC background accounts for about 10% and 25% of the sample, while the remaining events are genuine NC interactions, which also carry useful information for the ν_τ/ν_s discrimination.

These values are integrated over the energy. However, the residual ν_μ-CC background has a soft energy spectrum, since the rejection of ν_μ-CC events with a hard muon ($E_\mu >$ 1.5 GeV) is effective on high energy events (due to the flat y distribution of the CC interaction). The ν_e-CC background is mostly degraded to low visible energy, due to the coarse sampling of the detector which filters off the electro-magnetic component of the interaction. As a consequence the visible energy is mostly due to the residual hadronic component, as in the case of neutral current events.

The determination of the neutrino flight direction has been obtained by an automatic algorithm on the basis of the event topology and by taking advantage of the timing capabilities of the detector. The position of the centre of gravity of the event (as derived from the digital information) and of the earliest hits in the x and y views are determined along the z (vertical) direction, to establish whether they lay in the lowest or in the highest half of the event. The combined information of these variables is used to derive the flight direction of the neutrino. Moreover, these variables (event "vertex" and centre

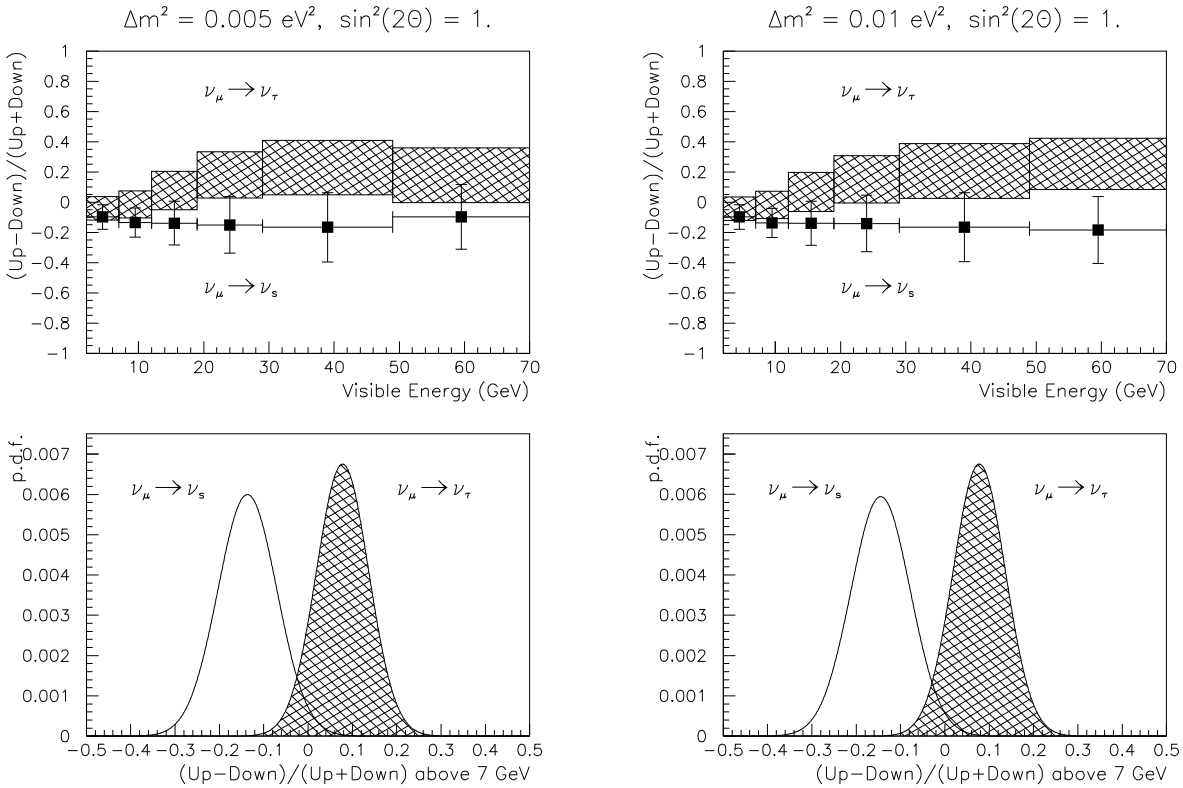

Figure 5.7: *Top:* Up/down asymmetry of muon-less events as a function of the visible energy, for maximal mixing and $\Delta m^2 = 5 \times 10^{-3}$ eV^2 (left) and $\Delta m^2 = 10^{-2}$ eV^2 (right). The expectations for $\nu_\mu \to \nu_\tau$ (hatched area) and for $\nu_\mu \to \nu_s$ oscillations (dots) are compared. Events have been generated with high statistics, error bars correspond to four years of data taking. The rightmost bin also integrates the contribution of events with reconstructed energy larger than 70 GeV. *Bottom:* Probability density function for the experimental outcome of the up/down asymmetry of events above 7 GeV after four years of data taking.

of gravity) provide a rough estimate of the neutrino zenith angle ($\simeq$ 20 degrees FWHM), which has been used to filter events near the horizontal. These events are of little use in the measurement of the up/down asymmetry since near the horizontal the up/down confusion and the ν_e background are larger and (in the upgoing sample) the oscillation probability is smaller.

The up/down discrimination algorithm is not yet as effective as the result of hand scanning and optimisation is in progress.

After rejection of events with a reconstructed zenith angle within 15 degrees from the horizontal, for which the determination of the neutrino direction is most ambiguous, the efficiency to muon-less ν_τ interactions is reduced to around 40%. On average 85% of the ν_τ-CC events have their sense of direction correctly assigned.

Fig. 5.7 shows the result of the outlined analysis. The differential up/down asymmetry

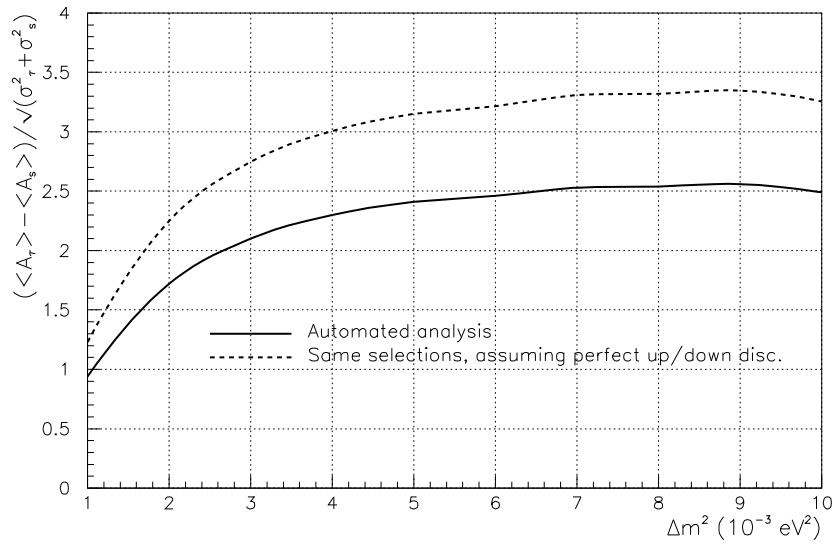

Figure 5.8: Significance of the ν_τ/ν_s separation in four years as a function of Δm^2.

of muon-less events as a function of the visible energy, defined as

$$A(E) = \frac{U(E) - D(E)}{U(E) + D(E)}, \tag{5.3}$$

with clear meaning of symbols, is shown for maximal mixing and $\Delta m^2 = 5 \times 10^{-3}$ eV^2 and 10^{-2} eV^2 for the two alternative oscillation hypotheses (top). In the $\nu_\mu \to \nu_\tau$ case there is an excess of muon-less events with high visible energy from the bottom hemisphere due to the τ decay into muon-less channels that produce neutral current like events and, hence, a positive asymmetry; in the $\nu_\mu \to \nu_s$ case there is a lack of neutral currents from the bottom hemisphere at all visible energies, since the sterile neutrino does not interact. At low energies a negative asymmetry is observed also in the $\nu_\mu \to \nu_\tau$ case. This is due to the residual background of ν_μ-CC events at small energies which gets depleted in the upgoing sample because of oscillations.

The figure also shows (bottom) the probability density functions for the experimental outcome for the up/down asymmetry of muon-less events of visible energies above 7 GeV. Results are given for four years of data taking: the two alternative hypotheses are discriminated at 90% (95%) C.L. with a rejection power of about 1% (3%).

Figure 5.8 shows the significance (number of sigmas) of the ν_τ/ν_s separation in four years, defined as the difference between the expectation values of the asymmetry for the two hypotheses normalised to the expected error. Below 3×10^{-3} eV^2 this method loses sensitivity, since it relies on high energy neutrinos which do not oscillate enough. At larger Δm^2, the separation achieved by the present analysis is at the 2.5σ level, mainly limited by the current performance of the up/down discrimination algorithm. For an equivalent efficiency to muon-less ν_τ interactions, hand scanning reduces the probability of a wrong classification by more than a factor 2. As shown in the figure, if a perfect up/down discrimination is assumed, a separation of more than 3σ on the same sample of muon-less events is obtained.

5.5 Comparison of different detector geometries

Alternative geometries, with vertical iron planes, have also been simulated, since they offer a better acceptance to neutrino interactions induced by a possible beam from CERN.

As far as atmospheric neutrinos are concerned, a structure with vertical planes presents acceptance limitations along the vertical, while it offers improved reconstruction capabilities for events near the horizontal. These latter events, however, have a limited L/E resolution as discussed in Chapter 3 (see equation (3.2)) and most of them are eliminated by the selection criteria. Fig. 5.9 compares the samples of selected fully contained events as a function of L/E for a structure with 8 cm iron planes oriented vertically or horizontally. The same set of reconstruction and kinematic criteria, along the lines discussed in section 5.3, has been applied in both cases. No specific selection against the cosmic muon background, which is more severe for the vertical layout, has been introduced.

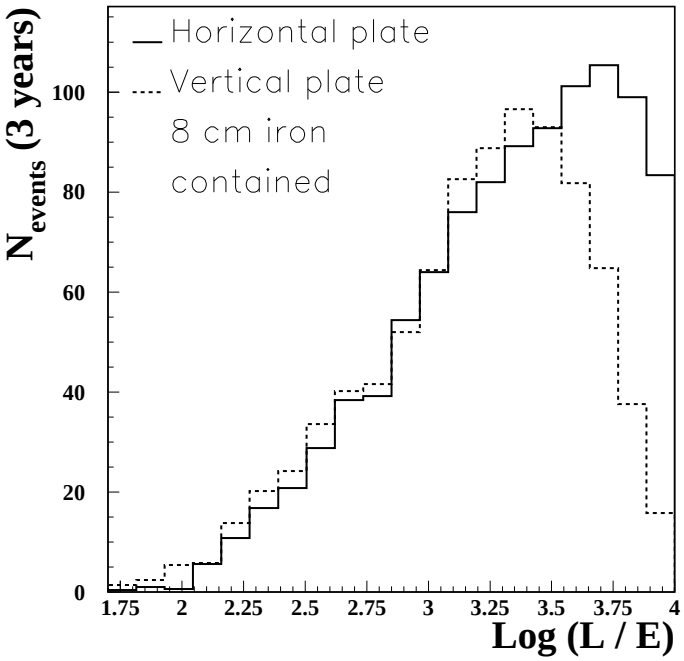

Figure 5.9: Comparison of the statistics of fully contained events selected with the vertical (dotted line) and horizontal (full line) layout. The loss in efficiency at large L/E is introduced by lower event reconstruction capabilities along the vertical direction.

The figure shows that, in the region where the first oscillation minimum would manifest itself, for all the values of Δm^2 allowed by Super-Kamiokande results, the statistics of selected events is similar in the two geometries, while at large L/E the effect of the limited acceptance along the vertical of the vertical structure is visible. This results in a reduced sensitivity to the mixing angle.

A more complete analysis has been performed with a more complex geometry, consisting of vertical iron planes 4 cm thick alternated with active planes of 2×2 cm^2

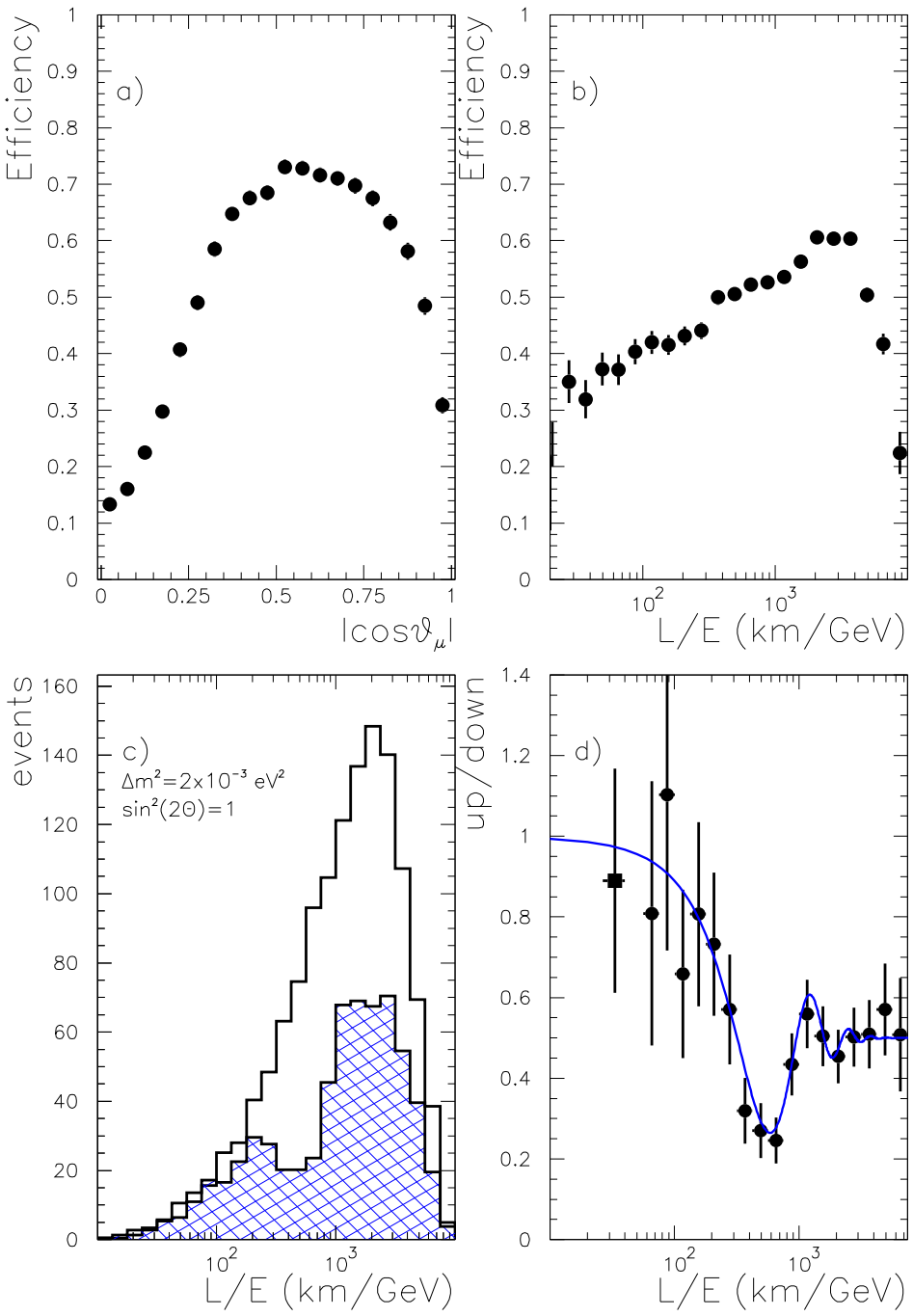

Figure 5.10: Results for a vertical plate design. *Top:* Efficiency versus $|\cos\theta_\mu|$ (a) and L/E (b): variables on the abscissa refer to the *true* variables and the normalisation is on the subset of events for which $P_\mu^{true} > 1.3\,\mathrm{GeV/c}$. *Bottom:* The L/E distribution for non-oscillated down-going muons (empty histogram) and oscillated up-going muons (dashed histogram) for maximal mixing and $\Delta m^2 = 2\times10^{-3}$ eV^2 (c) and their ratio (d) are shown.

iron/scintillators bars. The bars are oriented once vertically and once horizontally, to provide two coordinates. The ratio of the iron to the active element, the total weight and dimensions are similar to the baseline option discussed in the previous sections. A magnetic induction of 1.5 T of toroidal shape in the vertical iron planes has been assumed in the simulation. The muon reconstruction is obtained from a track fitting procedure, while the hadronic energy is obtained using the analog information from the scintillators.

An analysis along the lines described in section 5.3 has been performed, without any specific selection against the cosmic muon background, which is of particular importance when, as in this case, events with outgoing muons are included in the selected sample. An additional external veto is therefore assumed. Figures 5.10 a,b show the efficiency as a function of the muon angle and as a function of the L/E ratio. Figures 5.10 c,d show, for the value $\Delta m^2 = 2 \times 10^{-3}$ eV^2 and maximal mixing, the L/E distributions for up-going and down-going muons together with their ratio.

The above preliminary results show that, concerning the observation of the L/E pattern, the performances obtained with the vertical layout are similar to those obtained with the baseline solution.

5.6 Summary and conclusions

By exploiting the high energy component of the atmospheric muon neutrino fluxes, this experiment has the capability to detect the oscillation pattern from the comparison of L/E spectra of upgoing and downgoing neutrinos. The outlined analysis takes advantage of the up/down symmetry of the high energy atmospheric neutrino fluxes, which makes high energy atmospheric neutrinos an ideal source for disappearance experiments.

In the apparatus considered, the determination of the neutrino energy and direction relies mostly on the muon reconstruction. By means of the measurement of ν_μ disappearance, the existence of oscillations can be (dis)proved and the parameters measured over the entire range suggested by Super-Kamiokande and Kamiokande results (see fig. 5.6).

The comparison of rates of upward and downward muon-less events of high energy will allow to discriminate between oscillations into a sterile or a τ neutrino. A full simulation and analysis has been performed with the horizontal structure. The optimisation of the up/down separation, which represents the main experimental challenge, is still in progress. For $\Delta m^2 \geq 3 \times 10^{-3}$ eV^2, a separation at the 3σ level is within the reach of this experiment (see fig 5.8). For lower values of Δm^2 the separation of the two hypotheses is marginal, since the high energy component of the atmospheric neutrino fluxes does not oscillate enough.

Preliminary results on a vertical structure shows comparable capabilities in the detection of the L/E pattern, with a reduced acceptance at large L/E. A study of the ν_τ appearance with a vertical layout has not been performed yet.

$\nu_\tau - \nu_s$ discrimination using matter effects, as described in section 2.3, has not yet been addressed in detail for either detector structure. However, we believe that our massive magnetized calorimeter has a strong potential for this method of separation, for its ability to select large statistics of fully measured high energy up-going neutrino events. More generally, the capability to identify and fully measure separately ν_μ and $\bar{\nu_\mu}$ events is a very important feature of this detector.

Chapter 6

Potential Synergies with Other Experimental Programmes

6.1 Complementarity of atmospheric and long baseline programmes

The physics issues addressed by MONOLITH are fully complementary to the physics programme of the CERN neutrino beam to Gran Sasso (CNGS [18]). The main physics goal of the CNGS project is the experimental observation of τ appearance. This could be achieved either directly through the detection of the τ decay kink in nuclear emulsion [58] " à la CHORUS [59]", or indirectly through τ detection using kinematical criteria [60] " à la NOMAD [61]". However, the expected event rate is small since at L=730 km and E$\sim$15 GeV ν_μ oscillations, which are found to be maximal in atmospheric neutrinos, are not yet fully developed. It is therefore impossible to observe an oscillation pattern.

Furthermore, a similarly small τ appearance rate could also be obtained from fully developed oscillations at high Δm^2, but small mixing angle. Current limits from short baseline experiments [59, 61] do not exclude this possibility [23]. In the most extreme case, such a contribution could fully mask the effect of atmospheric $\nu_\mu - \nu_s$ oscillations in long baseline experiments, and mimick atmospheric $\nu_\mu - \nu_\tau$ oscillations. Here, MONOLITH could add some independent information, which would help in understanding these loopholes.

Earlier considerations of this complementarity have led to the suggestion of a detector concept which would combine the two physics programmes [62].

6.2 Studies in progress for neutrino beam from CERN to Gran Sasso

The baseline design of MONOLITH would have very limited sensitivity to the CNGS beam [18] due to the horizontal orientation of the detector planes and the direction of the magnetic field. Other designs with vertical plane orientation or vertical end caps are being studied which would be more suited to the beam. Such designs will be favourably considered if their performance on atmospheric neutrino measurements matches the performance of the baseline design.

The purpose of this section is to briefly investigate the potential physics issues which could be addressed with such a detector. No detailed simulations of potential beam performance have been made so far. One of the strengths of a 34 kt detector is its high event rate: with the upgraded CNGS beam performance [18], about 300.000 CC events with energies in the range 10-30 GeV could be expected in 4 years of running. Ideally, the presence of a near detector would allow to carry out the equivalent of the full physics programme discussed in [10] and [14]. Since a near detector pit is currently unaffordable, the remaining physics possibilities are unfortunately rather limited.

Based on the experience from previous beam simulations [64] we assume uncertainties of order 10% in the absolute beam flux prediction and its energy dependence. This makes any significant measurement of ν_μ disappearance almost impossible. Reversing the argument, the high event rate could be used to precisely measure the beam flux (modulated by oscillations). Once the oscillation parameters are known, for instance from the MONOLITH atmospheric neutrino measurements, this could reduce the beam uncertainties for τ appearance experiments.

Depending on the size of the associated systematic error, indirect measurements of τ appearance through the measurement of the NC/CC ratio might offer some possibilities. Previous measurements of this ratio for other purposes in high density calorimeters [63] have achieved systematic errors in the 0.5-1% range. However, all these results were obtained at neutrino energies of typically 50-100 GeV. Detailed studies are needed to establish the performance in the 10-30 GeV range, including the possibility to use the high event rate to study some of the systematic errors from the data themselves. Contrasting the expected error of a few % with the expected apparent NC/CC enhancement for $\nu_\mu - \nu_\tau$ oscillations ($\sim 1-20\%$ depending on Δm^2), it seems likely that a meaningful measurement can only be achieved if Δm^2 is large.

In conclusion, some beam measurements could be considered, but the absence of a near detector severely limits the physics possibilities. More quantitative studies are needed for a final evaluation.

6.3 Studies in progress for beams from muon storage rings

Neutrino beams from future muon storage rings [65] (neutrino factories) will be essentially pure beams of either $\nu_\mu + \bar{\nu}_e$ or $\bar{\nu}_\mu + \nu_e$. The occurence of $\nu_e - \nu_\mu$ or $\nu_e - \nu_\tau$ oscillations would therefore manifest itself via the appearance of wrong sign muons. A massive magnetized iron detector like MONOLITH, with good muon charge separation and momentum measurement, could therefore be well suited [66] for the observation of such oscillations. As pointed out in [67, 68] this kind of beams will in particular offer the possibility to measure the θ_{13} mixing angle, currently only constrained by Super-Kamiokande and CHOOZ results. It might also open the way for the study of CP violation in the neutrino system.

The performance of MONOLITH in such a beam would of course depend on the beam energy, intensity, distance from the source and on the beam direction. Given the very early status of the planning for such beams it would be premature to optimize the detector for such a possibility today. However, it might be interesting to consider that such a facility might become reality within the lifetime of the MONOLITH project, and that its useful life might be extended accordingly.

Chapter 7

Cost and Planning

The member institutions of the MONOLITH project will continue to pursue studies towards the realization of a full technical proposal. A detailed assignment of responsibilities for the detector construction and operation will be made in parallel to the finalization of the detector design.

Assuming a modular structure, the first part of the detector could be operational in 2002/2003. Total assembly time is expected to be 3 years.

Very preliminary cost estimates for the iron structure and the two basic detector options for a 34 kton detector are given in the next sections. The costs for installation, the full acquisition system and the general infrastucture strongly depend on the final design and are not yet included.

7.1 Iron and Magnet

The cost of the iron plates is estimated to be about 9 MEuro. This refers to 8 cm plates having the correct dimensions and precision to be assembled in 120 horizontal planes, and includes delivery to the Gran Sasso hall. The cost for the magnet coils is calculated to be about 0.5 MEuro for a field of order 1.2-1.4 T (see Appendix A). The cost for the active elements for such a structure is given in sections 7.2 or 7.3.

7.2 GSC option

The result of a preliminary study on the cost of the GSC option (54000 m^2 of Glass Spark Counters) is summarized in the following table:

- Glass Spark Counters	5 MEuro
- Strips	4 MEuro
- Front End Electronics	5 MEuro
- H.V. + power supplies	1.5 MEuro

The cost for the gas system has not yet been estimated.

7.3 Scintillator option

The preliminary estimate for the cost of the scintillator option (1.1 kton of scintillator in bars of 2×2 cm, 2-sided readout, 360000 channels) is summarized in the following table:

- Scintillator	12 MEuro
- WLS fibres (4 fibres/bar)	5 MEuro
- HPD	3 MEuro
- Electronics	2 MEuro

7.4 Summary

Adding the cost for the magnet and the detectors and allowing for some margin for installation and general infrastructure, a total cost estimate between 25 and 35 MEuro is obtained, depending upon the detector choice. More details will be known when the detector design has been finalized.

Chapter 8

Conclusion

We showed the feasability of a 34 kt magnetized iron detector which is able to

- measure the neutrino oscillation pattern in atmospheric neutrinos, therefore proving the oscillation hypothesis;
- improve the measurement of Δm^2 by almost an order of magnitude over previous measurements, covering the full currently allowed range;
- improve the discrimination between the $\nu_\mu - \nu_\tau$ and $\nu_\mu - \nu_s$ oscillation hypotheses. Depending on the oscillation parameters, this could be achieved through the measurement of the up/down ratio of NC-like events, through the presence or absence of a distortion of the oscillation pattern as a function of energy by matter effects, or through the (non)observation of an asymmetry in the oscillation patterns for neutrinos and antineutrinos.

Many of these measurements are unique to this detector, and therefore fully complementary to other planned neutrino physics programmes. They can be achieved on a relatively short timescale, at a cost which is dominated by the required detector mass. Furthermore, a detector of this kind might fit into even more ambitious long-term programmes for neutrino factories.

Acknowledgements

We wish to thank G. Battistoni and P. Lipari for very useful discussions and contributions. We are especially indebted with them for providing us with a high statistics sample of atmospheric neutrino interactions at the LNGS location. We also thank F. Pietropaolo for his invaluable contribution to the early stage of this work.

Appendix A
The magnetization of the iron plates

A.1 Introduction

Both the layout H and the layout V, introduced in the Section 4.2, are described by the scheme of the Fig. 8.1, that shows the layout H if read as a top view, and the layout V if read as a side view.

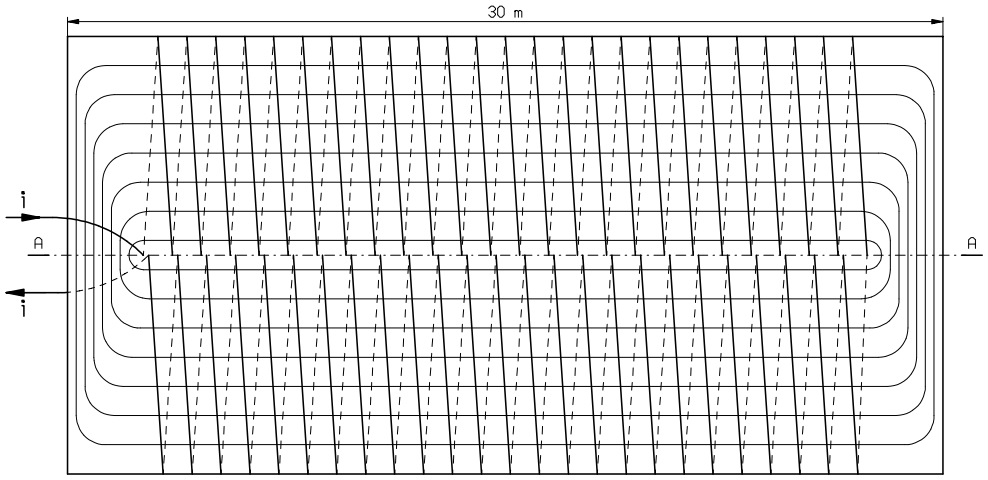

Figure 8.1: Simplified configuration of windings and field lines

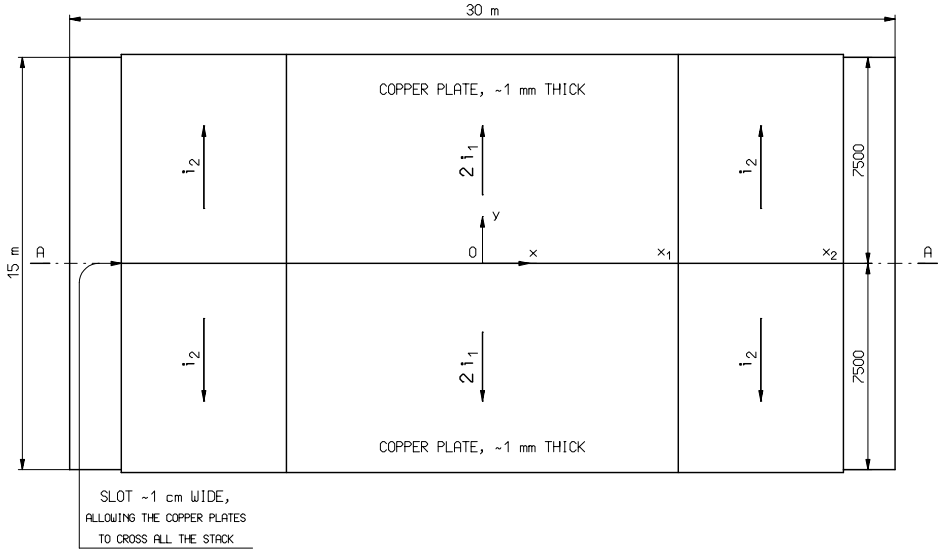

Figure 8.2: Layout H, top view of the stack

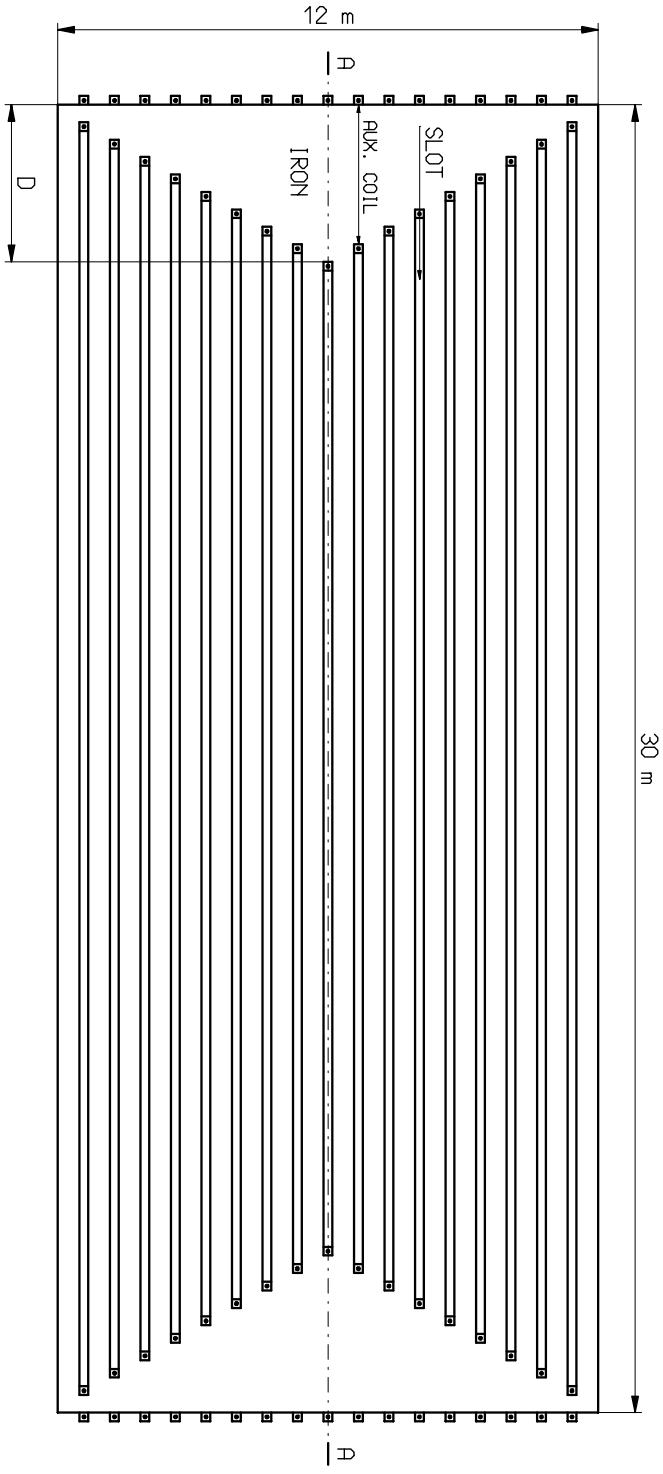

Figure 8.3: Layout V, simplified side-view of the stack, with the magnetic end-caps

A more realistic top view of the layout H is shown in the Fig. 8.2, where the field can be shaped, adjusting the total currents $4i_1$ and $4i_2$ and their boundaries, x_1 and x_2. Of course the total currents will be suitably subdivided by means of a corresponding subdivision and seriation of the copper plates carrying them.

In this layout the detectors cannot cross the *vertical* median plane A-A of the stack, because it contains the vertical conductors crossing the stack, so that the detectors have to transmit their signals to the far ends of the stack, located 30 m apart.

The Fig. 8.3 is a simplified side-view of the stack for the layout V, where the slots for the detectors are filled with iron near their ends, to obtain vertical paths for the field lines. The conductors of the Fig. 8.1 (not shown here for simplicity), carrying a total current $4i_1$, now cross the stack along the *horizontal* plane A-A, together with a layer of detectors. Here the shaping of the field is achieved with the help of auxiliary coils, carrying a total current $4i_2$. (In the Fig. 8.3 the cross sections of the auxiliary coils are shown as small squares with a dot in the centre).

The dead space taken by the end caps is of course fixed by their maximum thickness D, but D cannot be too small, because it has to be crossed by the same magnetic flux as half the thickness of the iron stack (60 x 80 mm = 4.8 m). If we decrease D, we have to increase the flux density B in the end caps, and approaching the saturation we have to increase too much the current i_2.

The magnetic fields for many configurations have been calculated by means of the programs of the package "POISSON SUPERFISH" [69]. With the layout V it is possible to obtain an almost uniform field in the iron plates, as shown in Fig. 8.4, where the bottom line is the trace of the plane A-A of the Fig. 8.3.

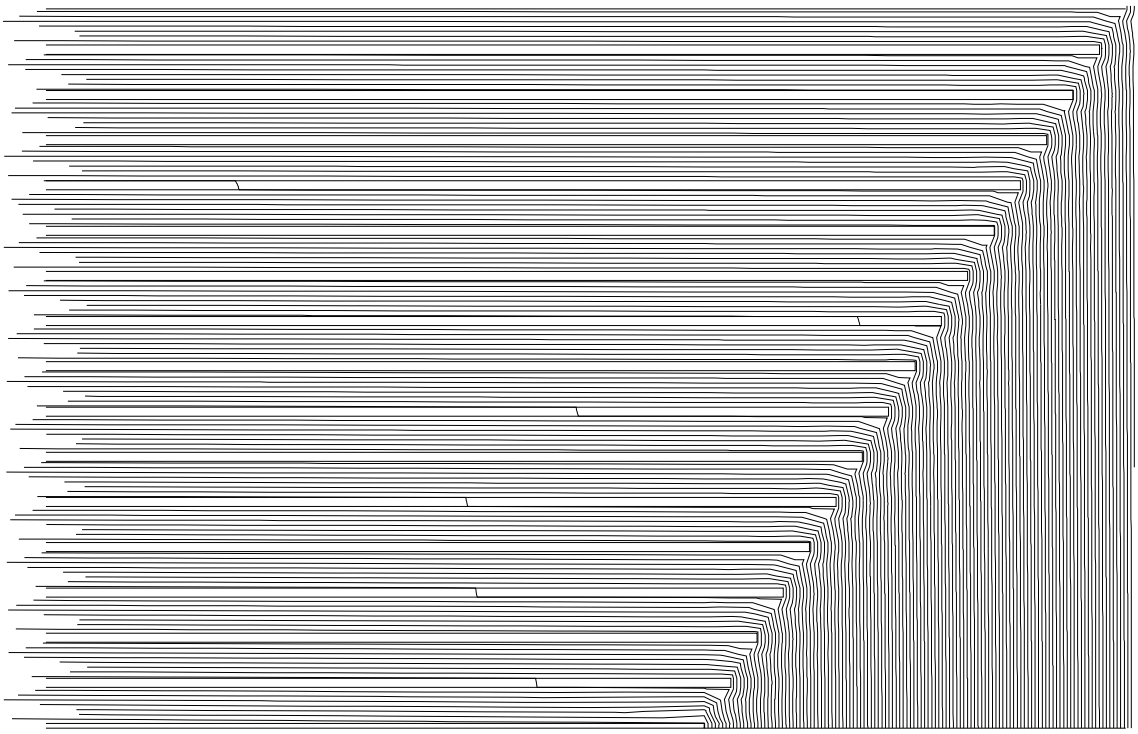

Figure 8.4: Layout V, field lines with $4i_1 = 28$ kA, $4i_2 = 60$ kA

The Fig. 8.5 shows the field lines in the first quadrant, for the layout H and a sample-set of values of x_1, x_2, i_1, i_2. The field lines cannot reach the corners of the iron planes, and we can consider as "dead space" the area of the corner where $|B|$ is smaller of 1 T.

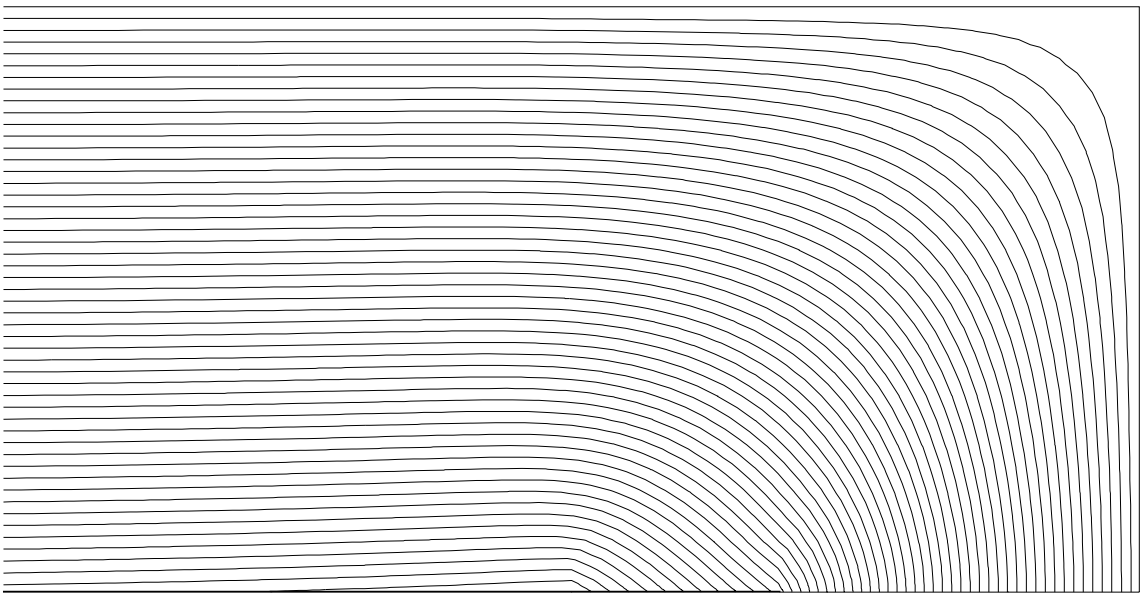

Figure 8.5: Layout H, field lines with $x_1 = 7.5$ m, $x_2 = 10.25$ m, $4i_1 = 60$ kA, $4i_2 = 120$ kA

A.2 Copper cost and power consumption

Following the considerations of the previous paragraph, we might obtain many interesting field configurations, but this would be useless without an evaluation of the cost of the windings and of the power consumption. To do this evaluation we introduce the following variables:

$$
\begin{aligned}
\rho &= 2 \cdot 10^{-8}\ \Omega\,\mathrm{m} = \text{resistivity of copper} \\
\kappa &= 8900\ \mathrm{kg/m^3} = \text{mass density of copper} \\
j &= \text{current density } (\mathrm{A/m^2}), \text{ constant for all the coils} \\
k &= \text{index of an individual coil} \\
i_k &= \text{current of coil } k \text{ (A)} \\
\ell_k &= \text{length of coil } k \text{ (m)} \\
s_k &= i_k/j = \text{cross section of coil } k \ (\mathrm{m^2}) \\
r_k &= \rho\,\ell_k/s_k = \rho\,\ell_k j/i_k = \text{resistance of coil } k \ (\Omega) \\
i &= \sum_k i_k = \text{total current (A)} \\
\ell &= \frac{1}{i}\sum_k \ell_k i_k = \text{mean coil length (m)} \\
W &= \sum_k r_k i_k^2 = \rho\, j \sum_k \ell_k i_k = \ell\, i \cdot \rho\, j = \text{total power consumption (W)}
\end{aligned}
$$

$$
\begin{aligned}
V &= \sum_k \ell_k s_k = \frac{1}{j}\sum_k \ell_k i_k = \ell\, i/j = \text{volume of the copper } (\mathrm{m}^3) \\
p_C &= \text{price of the copper, installed (Euro/kg)} \\
C_C &= \kappa\, V p_C = \ell\, i \cdot \kappa\, p_C/j = \text{total cost of the copper (Euro)} \\
p_J &= \text{price of the energy (Euro/J)} \\
p_E &= p_J \cdot 1000 \cdot 3600 = \text{price of the energy (Euro/kWh)} \\
Y &= \text{duration of the experiment (years)} \\
T &= Y \cdot 365 \cdot 24 \cdot 3600 = \text{duration of the experiment (s)} \\
C_E &= W \cdot T \cdot p_J = W \cdot 8.76 \cdot Y \cdot p_E = \ell\, i \cdot \rho\, j \cdot 8.76\, p_E\, Y = \\
&\qquad = \text{total cost of the energy consumption (Euro)} \\
C_T &= C_E + C_C = \ell\, i\, (8.76\, p_E\, Y \rho\, j + \kappa\, p_C/j) = \text{total}^1 \text{ cost of the magnetic field (Euro).}
\end{aligned}
$$

It can be easily shown that $C_T = C_E + C_C$ is minimum when $C_E = C_C$ and

$$
j = \sqrt{\frac{p_C\, \kappa}{8.76 \cdot p_E\, Y \rho}}\ .
$$

The cost of the energy, at the Gran Sasso, should be[2] about 0.08 Euro/kWh. The CERN estimate of p_C for a simple geometry corresponds to 36 Euro/kg. We can hope to get some saving on the construction cost, but, taking for the moment these values and a duration $Y = 5$ years, we obtain:

$$
j = 2.14 \cdot 10^6\, A/m^2 = 2.14\, \mathrm{A/mm}^2\,,
$$

$$
\rho\, j = 2 \cdot 10^{-8} \cdot 2.14 \cdot 10^6 = 0.0428\, \Omega\, \mathrm{A\, m}^{-1}\,,
$$

$$
\kappa\, p_C/j = 8900 \cdot 36/(2.14 \cdot 10^6) = 0.15\, \mathrm{Euro\, A}^{-1}\, \mathrm{m}^{-1}\ .
$$

Now we can easily calculate W and C_C:

$$
\begin{aligned}
W &= \ell\, i \cdot \rho\, j = \ell\, i \cdot 0.0428 \\
C_C &= \ell\, i \cdot \kappa\, p_C/j = \ell\, i \cdot 0.15\ .
\end{aligned}
$$

Inserting in these formulas the values of the total currents and of the mean coil lengths, respectively in kA and in m, we get for the most interesting configurations of the field, the corresponding values of W and C_C, respectively in kW and in kEuro (see the Table A.1).

[1] For the sake of simplicity, here we don't include in the calculation of C_T the cost of the power-supply, that roughly ranges from 40 to 150 kEuro when W ranges from 100 to 800 kW.

[2] Of course we have to consider this cost, though the Gran Sasso Laboratory does not use to charge the energy consumption to the experiments.

Table A.1

	ℓ_1 (m)	ℓ_2 (m)	$4i_1$ (kA)	$4i_2$ (kA)	$\lvert B\rvert$ (T)	dead space (%)	power cons. (kW)	copper cost (kEuro)
LAYOUT H	39	39	31	23	1.1	41	90	316
	39	39	24	56	1.3	11	134	468
	39	39	60	120	1.5	7	300	1053
LAYOUT V	42	34.8	20	14	1.12	16	57	199
$D = 4.8$ m	42	34.8	40	29	1.37	16	115	403
	42	34.8	80	57	1.52	16	229	802
	42	34.8	160	114	1.62	16	457	1603
$D = 3.6$ m	42	33.6	20	24	1.06	12	70	247
	42	33.6	28	60	1.20	12	137	479
	42	33.6	40	238	1.34	12	414	1452
	42	33.6	56	476	1.44	12	785	2752
	42	33.6	72	714	1.49	12	1156	4052
$D = 3$ m	42	33	20	60	1.01	10	121	423
	42	33	24	238	1.12	10	379	1329
	42	33	32	476	1.23	10	730	2558
	42	33	48	714	1.33	10	1095	3837

A.3 Conclusions

Looking at the Table A.1, we see that the second lines of the groups dedicated respectively to the layout H and to the layout V, with $D = 4.8$ m and with $D = 3.6$ m, correspond to situations satisfying the requirements on $|B|$ and on the power consumption and cost, indicated in the Section 4.2.

The better uniformity of the field and the better accessibility for the read-out of the detectors suggest the choice of the layout V.

The dead space indicated here refers to blind end-caps, but as mentioned earlier they could be structured and instrumented. At this point the choice between $D = 4.8$ m and $D = 3.6$ m could go towards the first value, because it permits a higher value of $|B|$.

Of course the discussions are far from being closed, and there will be no major problem in changing from one choice to another one.

Bibliography

[1] J.N. Bahcall, P.I. Krastev, and A.Yu. Smirnov, Phys. Rev. **D 59** (1999) 046002;
N. Hata and P. Langacker, Phys. Rev. **D 56** (1997) 6107;
V. Castellani et al., Phys. Rep. **281** (1997) 309.

[2] see e.g. G.L. Fogli et al., Phys. Rev. **D 55** (1997) 4385; Phys. Rev. **D 57** (1998) 5893.

[3] Super-Kamiokande Collaboration, Y. Fukuda et al., Phys. Rev. Lett. **81** (1998) 1562;
Super-Kamiokande Collaboration, Y. Fukuda et al., Phys. Lett. **B 436** (1998) 33;
Super-Kamiokande Collaboration, Y. Fukuda et al., Phys. Lett. **B 433** (1998) 9.

[4] LSND Collaboration, C. Athanassopoulos et al., Phys. Rev. Lett. **75** (1995) 2650;
J.E. Hill, Phys. Rev. Lett. **75** (1995) 2654;
LSND Collaboration, C. Athanassopoulos et al., Phys. Rev. **C 54** (1996) 2685;
LSND Collaboration, C. Athanassopoulos et al., Phys. Rev. Lett. **77** (1996) 3082;
LSND Collaboration, C. Athanassopoulos et al., Phys. Rev. **C 58** (1998) 2489;
LSND Collaboration, C. Athanassopoulos et al., Phys. Rev. Lett. **81** (1998) 1774.

[5] see e.g. J. Primack and A. Klypin, Nucl. Phys. Proc. Suppl. **51 B** (1996) 30.

[6] see e.g. S. Pakvasa, Invited talk at 8th International Workshop on Neutrino Telescopes, Venice, Italy, 23-26 Feb 1999, hep-ph/9905426, and references therein.

[7] V. Barger et al., hep-ph/9907421;
V. Barger et al., Phys. Rev. Lett. **82** (1999) 2640.

[8] G. Mannocchi et al., CERN/OPEN-98-004.

[9] A. Curioni et al., hep-ph/9805249;
M. Aglietta et al., LNGS-LOI 15/98, CERN/SPSC 98-28, SPSC/M615, Oct. 1998.

[10] NICE Letter of Intent, A. Baldini et al., LNGS-LOI 13/98 (1998);
M. Apollonio et al., CERN/SPSC 98-34, Oct. 1998.

[11] CHOOZ Collaboration, M. Apollonio et al., Phys. Lett. **B 420** (1998) 397;
CHOOZ Collaboration, M. Apollonio et al., hep-ex/9907037.

[12] Q.Y. Liu and A.Yu. Smirnov, Nucl. Phys. **B 524** (1998) 505;
E.J. Chun, C.W. Kim, and U.W. Lee, Phys. Rev. **D 58** (1998) 093003;
A.S. Joshipura and A.Yu. Smirnov, Phys. Lett. **B 439** (1998) 103;

M. Bando and K. Yoshioka, Prog. Theor. Phys. **100** (1998) 1239;
V. Barger et al., Phys. Rev. **D 58** (1998) 093016;
E.M. Lipmanov, Phys. Lett. **B 439** (1998) 119;
J.P. Bowes and R.R. Volkas, J. Phys. **G 24** (1998) 1249;
R. Foot and R.R. Volkas, Phys. Rev. **D 52** (1995) 6595;
R. Foot, Mod. Phys. Lett. **A 9** (1994) 169;
J. Bunn, R. Foot, R.R. Volkas, Phys. Lett. **B 413** (1997) 109;
A. Geiser, Phys. Lett. **B 444** (1999) 358;
M. Kobayashi, C.S. Lim and M.M. Nojiri, Phys. Rev. Lett. **67** (1991) 1685;
C. Giunti, C.W. Kim and U.W. Lee, Phys. Rev. **D 46** (1992) 3034;
W. Krolikowski, Acta Phys. Polon. **B 30** (1999) 227;
Y. Koide and H. Fusaoka, Phys. Rev. **D 59** (1999) 053004;
Y. Koide, Phys. Rev. **D 57** (1998) 5836.

[13] KEK proposal E-362, K2K (KEK to Kamioka) neutrino oscillation experiment at KEK-PS, hep-ex/9803014.

[14] The NUMI-MINOS Project, NUMI-L-375 report (may 98); The MINOS Detectors TDR, NUMI-L-337 report (october 98 version).

[15] Soudan-2:
M. Goodman, DPF Conference, UCLA (USA), january 99,
http://www.physics.ucla.edu/dpf99/trans/2-08.pdf;
W.A. Mann, Neutrinos Telescopes, Venice (Italy), february 99,
http://axpd24.pd.infn.it/transparencies/Mann.pdf.

[16] Kamiokande Collaboration, Y. Fukuda et al., Phys. Lett. **B 335** (1994) 237.

[17] CDHS Collaboration, F. Dydak et al., Phys. Lett. **B 134** (1984) 281;
CHARM Collaboration, F. Bergsma et al., Phys. Lett. **B 142** (1984) 103;
E776 Collaboration, L. Borodowsky et al., Phys. Rev. Lett. **68** (1992) 274;
KARMEN Collaboration, B. Zeitnitz et al., Prog. Part. Nucl. Phys.**40** (1998) 169;
Bugey Collaboration, B. Achkar et al., Nucl. Phys. **B 434** (1995) 503;
Krasnoyarsk Collaboration, G.S. Vidyakin et al., JETP Lett. **59** (1994) 237.

[18] K. Elsener (editor), CERN 98-02 and INFN/AE-98/05, May 1998;
R. Bailey et al., CERN-SL-99-034-DI, June 1999.

[19] S. Wojcicki, talk at Neutrino '98, Takayama, Japan, June 4-9, 1998.

[20] Particle Data Group, Eur. Phys. Journ. **C 3** (1998) 1.

[21] R. Foot, R.R. Volkas, and O. Yasuda, Phys. Rev. **D58** (1998) 013006;
M.C. Gonzalez-Garcia et al., Nucl. Phys. **B 543** (1999) 3.

[22] S.M. Bilenky et al., hep-ph/9906251.

[23] A. Geiser, Eur. Phys. J. **C 7** (1999) 437.

[24] C. Walter, talk given for the Super-Kamiokande Collaboration at EPS '99, Tampere, Finland, 15-21 July 1999.

[25] F. Vissani and A. Yu. Smirnov, Phys. Lett. B432 (1998) 376.

[26] J.W. Flanagan, J.G. Learned, and S. Pakvasa, Phys. Rev. **D 57** (1998) 2649; J.G. Learned, S. Pakvasa, and J.L. Stone, Phys. Lett. **B 435** (1998) 131.

[27] L. Wolfenstein, Phys. Rev. **D 17** (1978) 2369; Phys. Rev. **D 20** (1979) 2634.

[28] P. Lipari and L. Lusignoli, Phys. Rev. D, 58 (1998) 073005.

[29] F. Ronga for the MACRO Collaboration, hep-ex/9905025.

[30] S.P. Mikheyev and A.Y. Smirnov, Sov. J. Nucl. Phys. **42** (1985) 913; Nuovo Cimento **9C** (1986) 17.

[31] Q.Y. Liu, S.P. Mikheyev, and A.Y. Smirnov, Phys. Lett. **B 440** (1998) 319; M.V. Chizhov, S.T. Petcov, SISSA-28-99-EP and hep-ph/9903424.

[32] P.F. Harrison, D.H. Perkins, and W.G. Scott, Phys. Lett. **B 458** (1999) 79; and W.G. Scott, private communication

[33] A.A. Petrukhin, talk at the XIth Rencontres de Blois "Frontiers of Matter", Blois, France, June 28-July 3, 1999, and preprint MEPhI, No.006-99, 1999.

[34] S.I. Nikolsky, Nucl. Phys. B (Proc.Suppl.) **39A** (1995) 228.

[35] R.P. Kokoulin, A.A. Petrukhin, Sov. Journ. Part. and Nucl. **21** (1990) 332.

[36] O.C. Allkofer et al., Nucl. Phys. **B 259** (1985) 1; S. Matsuno et al., Phys. Rev. **D 29** (1984) 1.

[37] P. Picchi and F. Pietropaolo, "Atmospheric Neutrino Oscillations Experiments", ICGF RAP. INT. 344/1997, Torino 1997, (CERN preprint SCAN–9710037).

[38] P. Lipari, T. K. Gaisser and T. Stanev, Phys. Rev. **D 58** (1998) 073003.

[39] G. Battistoni and P. Lipari, hep-ph/9807475.

[40] G. Bencivenni et al., Nucl. Instr. and Method **A 300** (1991) 572.

[41] G. Bencivenni et al., Nucl. Instr. and Method **A 315** (1992) 507.

[42] M. De Deo et al., LNGS -95/39, June 1995.

[43] G. Bencivenni et al., Nucl. Instr. and Method **A 345** (1994) 456.

[44] G. Bencivenni et al., Nucl. Instr. and Method **A 332** (1993) 368.

[45] C. Gustavino et al., INFN/TC-99/14, submitted to Nucl. Instr. and Method.

[46] A. Abe et al.,"Glass RPC Module for Belle Endcap KL/mu Detector", Proc. of IV Int.Workshop on Resistive Plate Chamber and Related Detectors, Napoli, Oct 15-16 1997. Ed. Sergio Ratti, Riccardo de Asmundis.

[47] A. Skiba, Diploma Thesis, Hamburg University, October 1998.

[48] C. Hensel, Diploma Thesis, Hamburg University, October 1998.

[49] RD46 coll., P. Annis et al.:*A Single-Photon Multichannel Detector: the Megapixel EBCCD*, Proceedings of the SCIFI97 conference, Notre Dame, November 1997;
RD46 coll., P. Annis et al.:*High-resolution tracking using capillaries filled with liquid scintillator*, to be submitted to Nucl. Instr. and Method.

[50] see for instance:
LHCB technical proposal, CERN/LHCC-98-04, February 1998.

[51] K. Hoepfner, W. Schmidt-Parzefall: *Application of Liquid-Core Fibres for a Radiation-Hard Vertex Detector*, accepted for publication in Nucl. Instr. and Method.

[52] V. Agrawal, T.K. Gaisser, P. Lipari and T. Stanev, Phys. Rev. **D 53** (1996) 1314.

[53] M. Gluck, E. Reya and A. Vogt, Z. Phys. **C 67** (1995) 433.

[54] P. Lipari, M. Lusignoli and F. Sartogo, Phys. Rev. Lett. **74** (1995) 4384.

[55] GEANT Detector Description and Simulation Tools, CERN Program Library, Long Writeup W5013.

[56] A. Curioni and T. Tabarelli de Fatis, *Geometrical sampling of L/E distributions*, NOSEX-003/98, unpublished.

[57] T. Tabarelli de Fatis, *Oscillations and experimental resolution*, NOSEX-002/98, unpublished.

[58] OPERA letters of intent,
S. Shibuya et al., CERN-SPSC/97-24, SPSC/I 218, LNGS-LOI 8/97 (1997);
K. Kodama et al., CERN/SPSC 98-25, SPSC/M612, LNGS-LOI 8/97, Add. 1.

[59] CHORUS Collaboration, E. Eskut et al., Phys. Lett. **B 424** (1998) 202;
CHORUS Collaboration, E. Eskut et al., Phys. Lett. **B 434** (1998) 205.

[60] ICARUS Collaboration, P. Benetti et al., Nucl. Instr. Methods **A 327** (1993) 327; **A 332** (1993) 332; P. Cennini et al., Nucl. Instr. Methods **A 333** (1993) 567; **A 345** (1994) 230; **A 355** (1995) 355;
ICARUS-CERN-Milano Collaboration, CERN/SPSLC 96-58, SPSLC/P 304, December 1996.

[61] NOMAD Collaboration, J. Altegoer et al., Phys. Lett. **B 431** (1998) 219;
NOMAD Collaboration, P. Astier et al., Phys. Lett. **B 453** (1999) 169.

[62] K. Winter et al., *Expression of Interest to participate in the Study, Construction and Use of a Neutrino Facility at the Gran Sasso Laboratory*, CERN/SPSC 98-36; SPSC-M623.

[63] CCFR Collaboration, K.S. McFarland et al., Eur. Phys. J. **C 1** (1998) 509;
CCFR Collaboration, C.G. Arroyo et al., Phys. Rev. Lett. **72** (1994) 3452;
CCFR Collaboration, P.G. Reutens et al., Z. Phys. **C 45** (1990) 539;
CDHS Collaboration, A. Blondel et al., Z. Phys. **C 45** (1990) 361;
CHARM Collaboration, J.V. Allaby et al., Z. Phys. **C 36** (1987) 611.

[64] G. Collazuol et al., presented at NOW98 workshop, Amsterdam, 7-9 September 1998, CERN OPEN-98-032.

[65] D. Cline and D. Neuffer, AIP Conf. Proc. **68** (1980) 846; reproduced in AIP Conf. Proc. **352** (1996) 10;
S. Geer, Phys. Rev. **D 57** (1998) 6989; Erratum-ibid. D 59 (1999) 039903.

[66] J.J. Gomez-Cadenas and A. Cervera-Villanueva, talks given at ν-Fact '99, Lyon, 5-9 July 1999.

[67] A. De Rujula, M.B. Gavela and P. Hernandez, Nucl. Phys. **B 547** (1999) 21.

[68] V. Barger, S. Geer and K. Whisnant, hep-ph/9906487.

[69] J.H. Billen, L.M. Young, *POISSON SUPERFISH*, LA-UR-96-1834, Los Alamos National Laboratory, Revised November 14, 1998.